

Tri-Domain Multiuser MIMO Precoding Optimization and Channel Estimation with Spatial-EM Reconfigurable Antenna

Yining Li, Ziwei Wan, Zhen Gao, *Senior Member, IEEE*, Keke Ying, Lipeng Zhu, *Member, IEEE*, and Rui Zhang, *Fellow, IEEE*

Abstract—In this paper, we propose a tri-domain reconfigurable multiuser multiple-input multiple-output (MIMO) communication system that integrates the electromagnetic (EM) reconfigurable antenna (EMRA) with the spatially movable antenna (SMA), termed the spatial-EM reconfigurable antenna (SEMRA). The proposed system offers EM, spatial, and digital domain degrees of freedom (DoFs) for joint channel reconfiguration, yet introduces new challenges in channel estimation (CE) and precoding optimization. Specifically, for multiuser orthogonal frequency division multiplexing (OFDM) downlink, the precoding design is formulated as a tri-domain optimization problem over antenna positions, EM-domain radiation-pattern weights, and digital precoders. We first develop a zero-forcing (ZF)-based baseline algorithm to decouple the design of spatial reconfiguration, and then propose a weighted minimum mean square error (WMMSE)-based tri-domain joint optimization algorithm for further improving the spectral efficiency (SE). Furthermore, we propose a low-overhead movement-aided channel estimation scheme in which coordinated antenna repositioning across pilot slots synthesizes a denser virtual array, enabling more accurate angle-of-departure (AoD) estimation and EM-domain channel state information (eCSI) reconstruction under the same per-user pilot overhead as the EMRA baseline. The resulting parametric representation enables eCSI assembly at desired antenna positions without additional pilots. Simulation results show that the proposed CE scheme improves eCSI estimation accuracy and the proposed SEMRA achieves higher SE than the EMRA baseline under the same pilot overhead.

Index Terms—Spatial-EM reconfigurable antenna, channel estimation, precoding, spectral efficiency, tri-domain hybrid precoding, weighted minimum mean square error.

I. INTRODUCTION

Future wideband multiuser wireless systems require higher spectral efficiency (SE) under increasingly tight hardware constraints [1], [2]. In traditional fixed-antenna (TFA) settings, performance is improved mainly through digital precoding and array scaling, whereas antenna locations and radiation patterns remain largely fixed after fabrication. This limitation has motivated growing interest in flexible hardware architectures that introduce new physical-layer degrees of freedom (DoFs). Prior work on reconfigurable intelligent surfaces (RIS) has demonstrated the promise of programmable propagation environments [3], yet its passive nature also brings cascaded-channel acquisition and double-fading penalties, complicating practical deployment [4]. On the other hand, active transceiver architectures [5], [6], such as multiple-input multiple-output (MIMO) systems with electromagnetic reconfigurable antenna (EMRA), have shown substantial SE improvement without

extra antennas or power-hungry radio-frequency (RF) chains. More recently, spatially movable antenna (SMA) architectures, including movable antenna (MA) [7], [8] and fluid antenna systems (FAS) [6], [9], have emerged to unlock additional spatial DoFs for MIMO communications. Although EMRA and SMA have each attracted much attention, their integration remains largely underexplored [10].

A. Prior Work

For EMRA architectures, one appealing benefit is the ability to adapt the radiation field [11]–[13]. By electronically tuning loads or switch states, the current distribution of each antenna element can be changed, thereby reshaping its radiation pattern. At the system level, this effect can be modeled through antenna-mode selection or basis-function expansions whose coefficients serve as electromagnetic (EM)-domain precoders [13]–[15]. In this setting, transmitter design depends not only on conventional spatial-domain channel state information (sCSI), but also on EM-domain channel state information (eCSI), which links the propagation geometry to the radiation-pattern basis and enables joint EM-domain and digital-domain precoding for substantial SE improvement over TFA systems [13], [15].

One core challenge for EMRA systems is channel estimation (CE). Recent studies have also examined channel state information (CSI) extrapolation across radiation states [16]. In wideband parametric CE pipelines, the channel is first characterized by multipath delays, angle-of-departure (AoD), angle-of-arrival (AoA), and equivalent path gains, and the eCSI required for EM-domain design is then reconstructed from these geometric parameters [12], [15], [17], [18]. Although this representation reduces the estimation dimension, its accuracy still hinges on spatial sampling. In orthogonal frequency division multiplexing (OFDM) systems, frequency diversity mainly assists delay estimation, whereas reliable AoD recovery still requires sufficiently rich spatial observations and is further affected by spatial-wideband and frequency-wideband effects [19]. For fixed-geometry arrays, simply enlarging the inter-element spacing is not always effective. Although a larger aperture can improve angular resolution, excessive spacing may also introduce spatial aliasing and grating-lobe ambiguity [17], [18]. Since AoD errors directly perturb the steering and basis matrices used to assemble eCSI, they propagate to EM-domain precoding and degrade the subsequent transmission design [15], [20], [21].

On the other hand, research on SMA architectures, including MA and FAS, has expanded rapidly. Existing work covers channel modeling, transmission design, position optimization, and weighted minimum mean square error (WMMSE) precoding [7], [22]–[24], with surveys in [8], [9]. This line has recently been extended to 6D movable antenna (6DMA) systems, which augment translation with rotations and thus add position-and-orientation DoFs [25]. CE methods for position-flexible systems include linear minimum mean square error (LMMSE)-type and Bayesian approaches [26], [27]. However, these studies mainly use movement or orientation control to enhance transmission or recover sCSI, e.g., via field interpolation, channel-map recovery, or port selection, rather than to aid AoD-driven eCSI reconstruction for EM-domain precoding [28].

Recent studies have started to connect spatial and electromagnetic reconfiguration [10], but mostly through electronically synthesized discrete radiation locations rather than physical antenna repositioning. For example, pixel-based reconfigurable antennas have been proposed to emulate FAS ports on a fixed aperture [29], and the reconfigurable pixel antenna (RPA)-based electronic movable-antenna array (RE-MAA) further turns this equivalent-movement idea into multiuser communication design by selecting from a finite set of candidate radiation positions [30]. Likewise, radiation-center reconfigurable antenna arrays and their tri-hybrid beamforming architecture treat the EM layer as discrete radiation-center selection combined with analog and digital beamforming [31]. These works demonstrate the promise of combining spatial and EM adaptability, but the spatial flexibility they exploit is still realized through discrete equivalent-position or radiation-center selection rather than physical antenna repositioning. More importantly, they mainly focus on beamforming or antenna-state selection under a given observation geometry, without exploiting spatial reconfiguration during CE to synthesize denser virtual arrays for improved AoD estimation and eCSI reconstruction.

This gap motivates the present work. What is still missing in the literature is a unified spatial-EM reconfigurable antenna (SEMRA) architecture that uses physical antenna repositioning during CE as a sensing mechanism for AoD-driven eCSI reconstruction, while retaining EM-domain reconfigurability for transmission design. The proposed SEMRA architecture fills this gap by using coordinated antenna repositioning across pilot slots to synthesize a denser virtual array under the same per-user pilot overhead as the EMRA baseline, after which the reconstructed eCSI supports tri-domain hybrid precoding over antenna positions, EM-domain pattern weights, and digital precoders.

B. Contributions

Motivated by the above, this paper proposes a unified SEMRA framework that combines tri-domain precoding with movement-aided parametric CE. The main idea is to jointly exploit spatial reconfiguration and EM-domain reconfigurability. Spatial reconfiguration is used not only for antenna position optimization at the transmitter, but also as a channel

sensing mechanism for virtual-array-assisted eCSI reconstruction, while EM-domain pattern adaptation is retained for transmission design. The main contributions are summarized as follows.

- Within the proposed SEMRA framework, we develop a concrete low-overhead movement-aided parametric CE procedure. By coordinating local repositioning of the $M_y \times M_z$ antennas over N_s pilot slots, a denser virtual array is synthesized while preserving the same per-user pilot overhead as the EMRA baseline. The resulting virtual array supplies additional spatial samples for the parametric estimation pipeline, improves AoD estimation, and yields a position-independent parametric channel model from which the eCSI can be assembled at desired antenna positions without additional pilots.
- We formulate the SEMRA SE-maximization problem and develop a tri-domain alternating optimization framework based on block coordinate descent (BCD) over antenna positions, EM-domain pattern weights, and digital precoders. A zero-forcing (ZF)-based joint design is first constructed as a low-complexity baseline to isolate the gain of spatial reconfiguration beyond existing EM-digital designs for EMRA systems. We then develop a WMMSE-based design to further improve the system SE.
- Numerical results show that the proposed CE scheme improves eCSI accuracy over the EMRA baseline under the same per-user pilot overhead. Within the tested range, both SEMRA-ZF and SEMRA-WMMSE achieve higher SE than the EMRA baseline under both estimated and perfect eCSI scenarios, and SEMRA-WMMSE further improves over SEMRA-ZF. The SEMRA-over-EMRA advantage is especially evident at larger inter-element spacings, where the EMRA baseline is more sensitive to spatial aliasing. Even when the spatial degree of freedom is restricted to a discrete per-antenna port codebook, SEMRA still attains most of the gain of the continuous design, suggesting practical robustness to hardware-induced position discretization.

Notation: Matrices and column vectors are denoted by uppercase and lowercase boldface letters, respectively. $(\cdot)^T$, $(\cdot)^*$, $(\cdot)^H$, $(\cdot)^{-1}$, $(\cdot)^\dagger$, and $\mathbb{E}\{\cdot\}$ denote the transpose, conjugate, Hermitian transpose, inversion, Moore-Penrose pseudoinverse, and expectation. $[\mathbf{x}]_k$ and $[\mathbf{A}]_{i,j}$ denote the k -th entry of vector \mathbf{x} and the (i, j) -th entry of matrix \mathbf{A} . $\text{diag}(\mathbf{a})$ forms a diagonal matrix from vector \mathbf{a} , and $\text{Blkdiag}\{\mathbf{a}_1, \dots, \mathbf{a}_M\}$ constructs a block diagonal matrix. \odot denotes the Hadamard product. $\|\cdot\|_2$ and $\|\cdot\|_F$ denote the ℓ_2 norm and Frobenius norm, respectively. $\Re\{\cdot\}$ and $\Im\{\cdot\}$ denote the real and imaginary parts, respectively. j is the imaginary unit. \mathbf{I}_N denotes the $N \times N$ identity matrix. $\mathcal{CN}(\mu, \sigma^2)$ denotes a complex Gaussian distribution.

II. SYSTEM MODEL AND PROBLEM FORMULATION

A. Downlink Signal Model

We consider a time-division duplex (TDD) multiuser MIMO-OFDM downlink system implemented with the SEMRA architecture illustrated in Fig. 1. The base station

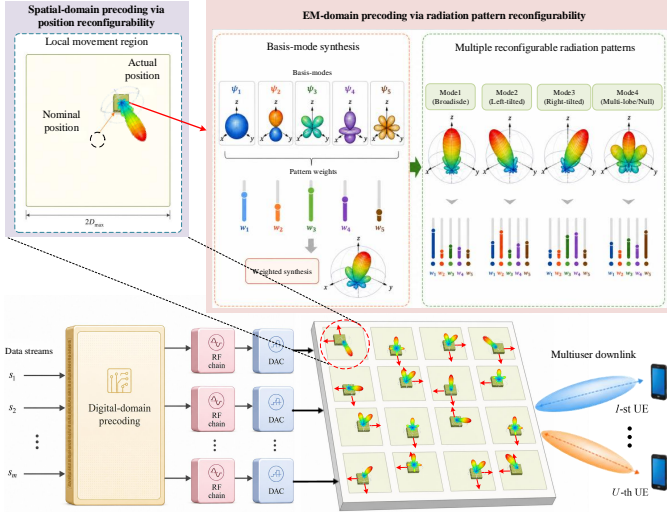


Fig. 1. SEMRA-enabled multiuser downlink with EM-domain radiation-pattern reconfigurability and spatial-domain position reconfigurability.

(BS) employs an $M = M_y M_z$ uniform planar array (UPA) of SEMRA elements to serve U single-antenna user equipments (UEs), each with a fixed position and radiation pattern. The inter-element spacings of the UPA along the y - and z -axes are d_y and d_z , respectively. The number of OFDM subcarriers is G with subcarrier spacing $\Delta f \triangleq B_w/G$, and $f_g \triangleq (g-1)\Delta f$ ($1 \leq g \leq G$) denotes the frequency of the g -th subcarrier. The received signal at the u -th UE ($1 \leq u \leq U$) and the g -th subcarrier ($1 \leq g \leq G$) is given by

$$y_{u,g} = \mathbf{h}_{u,g}^H \mathbf{W}_g \mathbf{s}_g + n_{u,g}, \quad (1)$$

where $\mathbf{h}_{u,g} = [h_{u,1,g}, \dots, h_{u,M,g}]^T \in \mathbb{C}^M$ is the downlink channel vector between the BS and the u -th UE, $\mathbf{W}_g = [\mathbf{w}_{1,g}, \dots, \mathbf{w}_{U,g}] \in \mathbb{C}^{M \times U}$ is the digital precoding matrix with $\mathbf{w}_{u,g} \in \mathbb{C}^{M \times 1}$ denoting the digital precoder vector for the u -th UE on the g -th subcarrier, $\mathbf{s}_g \in \mathbb{C}^U$ is the data symbol vector satisfying $\mathbb{E}\{\mathbf{s}_g \mathbf{s}_g^H\} = \mathbf{I}_U$, and $n_{u,g} \sim \mathcal{CN}(0, \sigma_n^2)$ is additive white Gaussian noise (AWGN).

B. Channel Model

The channel between the m -th BS antenna and the u -th UE on the g -th subcarrier is modeled as [32]

$$h_{u,m,g} = \sum_{i=1}^{L_u} \tilde{x}_{i,u} f_{\text{rx},u}(\vartheta_{i,u}, \varphi_{i,u}) f_{\text{tx},m}(\theta_{i,u}, \phi_{i,u}) \times e^{-j \frac{2\pi}{\lambda} (\mathbf{k}_{\text{tx},i,u}^T \mathbf{p}_m + \mathbf{k}_{\text{rx},i,u}^T \mathbf{r}_u)} \cdot e^{-j 2\pi \tau_{i,u} f_g}, \quad (2)$$

where L_u is the number of channel paths, $\tilde{x}_{i,u}$ and $\tau_{i,u}$ denote the complex gain and delay of the i -th path, respectively, $(\theta_{i,u}, \phi_{i,u})$ and $(\vartheta_{i,u}, \varphi_{i,u})$ are respectively the AoD and AoA, $f_{\text{tx},m}(\cdot)$ and $f_{\text{rx},u}(\cdot)$ denote the real-valued scalar radiation-pattern gains of the BS and UE antennas, respectively, and \mathbf{p}_m , \mathbf{r}_u are the position vectors of BS antenna m and UE u , respectively. Throughout this paper, the BS-side departure azimuth is restricted to the front half-space, i.e., $\phi_{i,u} \in [-\pi/2, \pi/2]$. The unit direction vectors $\mathbf{k}_{\text{tx},i,u}, \mathbf{k}_{\text{rx},i,u} \in \mathbb{R}^3$ are defined as $\mathbf{k}_{\text{tx},i,u} = [\sin \theta_{i,u} \cos \phi_{i,u}, \sin \theta_{i,u} \sin \phi_{i,u}, \cos \theta_{i,u}]^T$ and $\mathbf{k}_{\text{rx},i,u} = [\sin \vartheta_{i,u} \cos \varphi_{i,u}, \sin \vartheta_{i,u} \sin \varphi_{i,u}, \cos \vartheta_{i,u}]^T$.

Incorporating the delay into the path gain as $x_{i,u,g} = \tilde{x}_{i,u} e^{-j 2\pi \tau_{i,u} f_g}$, the channel can be written in the compact matrix form as

$$\mathbf{h}_{u,m,g} = \mathbf{f}_{\text{rx},u}^T \mathbf{A}_u \boldsymbol{\Sigma}_{u,g} \mathbf{B}_{u,m} \mathbf{f}_{\text{tx},u,m}, \quad (3)$$

where $\mathbf{f}_{\text{rx},u} \in \mathbb{R}^{L_u}$ and $\mathbf{f}_{\text{tx},u,m} \in \mathbb{R}^{L_u}$ collect the receive and transmit pattern gains along all L_u paths, with the i -th elements being $f_{\text{rx},u}(\vartheta_{i,u}, \varphi_{i,u})$ and $f_{\text{tx},m}(\theta_{i,u}, \phi_{i,u})$, respectively, $\mathbf{A}_u = \text{diag}(\mathbf{a}_u) \in \mathbb{C}^{L_u \times L_u}$ and $\mathbf{B}_{u,m} = \text{diag}(\mathbf{b}_{u,m}) \in \mathbb{C}^{L_u \times L_u}$ capture the array steering phases, with $[\mathbf{a}_u]_i = e^{-j \frac{2\pi}{\lambda} \mathbf{k}_{\text{rx},i,u}^T \mathbf{r}_u}$ and $[\mathbf{b}_{u,m}]_i = e^{-j \frac{2\pi}{\lambda} \mathbf{k}_{\text{tx},i,u}^T \mathbf{p}_m}$, and $\boldsymbol{\Sigma}_{u,g} = \text{diag}([x_{1,u,g}, \dots, x_{L_u,u,g}]) \in \mathbb{C}^{L_u \times L_u}$ collects the per-path gains.

C. EM-Domain CSI Representation

To enable EM-domain radiation pattern optimization, we represent the transmit pattern as a weighted combination of K orthonormal basis functions

$$f_{\text{tx},m}(\theta, \phi) = \sum_{k=1}^K \alpha_{k,m} \omega_k(\theta, \phi), \quad (4)$$

where $\{\omega_k(\theta, \phi)\}_{k=1}^K$ are real-valued orthonormal basis functions over the unit sphere, constructed from real spherical harmonics as detailed in [15]. The orthonormality condition reads $\int_0^{2\pi} \int_0^\pi \omega_k(\theta, \phi) \omega_{k'}(\theta, \phi) \sin \theta d\theta d\phi = \delta_{k,k'}$, and $\boldsymbol{\alpha}_m = [\alpha_{1,m}, \dots, \alpha_{K,m}]^T \in \mathbb{R}^K$ is the weight coefficient vector for the m -th antenna. Under the adopted decomposition, $f_{\text{tx},m}(\theta, \phi)$ models the real-valued directional gain, and we further assume that $\|\boldsymbol{\alpha}_m\|_2 = 1$. Applying (4) to the transmit pattern gain vector yields

$$\mathbf{f}_{\text{tx},u,m} = \boldsymbol{\Omega}_u \boldsymbol{\alpha}_m \in \mathbb{C}^{L_u}, \quad \forall u, m, \quad (5)$$

where $\boldsymbol{\alpha}_m$ parameterizes real gain-pattern coefficients, and the (i, k) -th element of $\boldsymbol{\Omega}_u \in \mathbb{R}^{L_u \times K}$ is $[\boldsymbol{\Omega}_u]_{i,k} = \omega_k(\theta_{i,u}, \phi_{i,u})$. Substituting (5) into (3), the channel can be expressed as

$$\mathbf{h}_{u,m,g} = \mathbf{f}_{\text{rx},u}^T \mathbf{A}_u \boldsymbol{\Sigma}_{u,g} \mathbf{B}_{u,m} \boldsymbol{\Omega}_u \boldsymbol{\alpha}_m = \mathbf{q}_{u,m,g}^H \boldsymbol{\alpha}_m. \quad (6)$$

We define the eCSI vector as

$$\mathbf{q}_{u,m,g}^H \triangleq \mathbf{f}_{\text{rx},u}^T \mathbf{A}_u \boldsymbol{\Sigma}_{u,g} \mathbf{B}_{u,m} \boldsymbol{\Omega}_u \in \mathbb{C}^{1 \times K}, \quad (7)$$

and define the corresponding position-independent equivalent channel gain vector as

$$\boldsymbol{\chi}_{u,g} \triangleq (\mathbf{f}_{\text{rx},u}^T \mathbf{A}_u \boldsymbol{\Sigma}_{u,g})^H \in \mathbb{C}^{L_u}. \quad (8)$$

It collects the position-independent UE-side and path-gain terms. The corresponding column-vector form of the eCSI is $\mathbf{q}_{u,m,g} = \boldsymbol{\Omega}_u^T \mathbf{B}_{u,m}^H \boldsymbol{\chi}_{u,g} \in \mathbb{C}^{K \times 1}$.

By aggregating the eCSI across all M antennas, we define the stacked eCSI vector $\mathbf{q}_{u,g} \triangleq [\mathbf{q}_{u,1,g}^T, \dots, \mathbf{q}_{u,M,g}^T]^T \in \mathbb{C}^{MK \times 1}$ and its conjugated form $\bar{\mathbf{q}}_{u,g} \triangleq \mathbf{q}_{u,g}^*$. We also define the block-diagonal EM precoding matrix $\boldsymbol{\Lambda} \triangleq \text{Blkdiag}\{\boldsymbol{\alpha}_1, \dots, \boldsymbol{\alpha}_M\} \in \mathbb{R}^{MK \times M}$. The effective channel then satisfies

$$\mathbf{h}_{u,g}^H = \bar{\mathbf{q}}_{u,g}^H \boldsymbol{\Lambda}. \quad (9)$$

Substituting (9) into (1) yields $y_{u,g} = \bar{\mathbf{q}}_{u,g}^H \mathbf{\Lambda} \mathbf{W}_g \mathbf{s}_g + n_{u,g}$, so the signal-to-interference-plus-noise ratio (SINR) for the u -th UE on the g -th subcarrier is

$$\text{SINR}_{u,g} = \frac{|\bar{\mathbf{q}}_{u,g}^H \mathbf{\Lambda} \mathbf{w}_{u,g}|^2}{\sum_{\substack{\ell=1 \\ \ell \neq u}}^U |\bar{\mathbf{q}}_{u,g}^H \mathbf{\Lambda} \mathbf{w}_{\ell,g}|^2 + \sigma_n^2}. \quad (10)$$

Accordingly, the sum SE is given by

$$R = \sum_{g=1}^G \sum_{u=1}^U \log_2(1 + \text{SINR}_{u,g}). \quad (11)$$

D. SEMRA Model and Problem Formulation

Unlike the EMRA with TFA architecture, the proposed SEMRA architecture jointly optimizes the per-antenna EM-domain pattern weights α_m and antenna positions \mathbf{p}_m . Let $\bar{\mathbf{p}}_m$ denote the reference position of the m -th antenna in the reference UPA. In SEMRA, each transmit antenna is permitted to move within a local feasible region \mathcal{S}_m centered at $\bar{\mathbf{p}}_m$ (depicted as the local movement region in Fig. 1), which is defined as

$$\mathcal{S}_m \triangleq \{\mathbf{x} \in \mathbb{R}^3 \mid \|\mathbf{x} - \bar{\mathbf{p}}_m\|_\infty \leq D_{\max}, [\mathbf{x}]_1 = 0\}, \quad (12)$$

where D_{\max} is the maximum allowable displacement for each antenna. To avoid antenna collisions, we require a minimum inter-antenna separation $D_{\text{sep}} > 0$ over all feasible positions, which is ensured for the reference UPA if $d_y \geq 2D_{\max} + D_{\text{sep}}$ and $d_z \geq 2D_{\max} + D_{\text{sep}}$. The position \mathbf{p}_m enters the channel through the BS-side steering matrix $\mathbf{B}_{u,m}$ in (3), introducing an additional spatial degree of freedom for performance optimization.

According to (9), the effective channels are jointly determined by the antenna positions $\mathbf{p} \triangleq [\mathbf{p}_1^T, \dots, \mathbf{p}_M^T]^T \in \mathbb{R}^{3M}$ and the per-antenna EM-domain weights α_m , whose effects are captured by $\bar{\mathbf{q}}_{u,g}$ and $\mathbf{\Lambda}$, respectively. Let $\mathbf{W} \triangleq \{\mathbf{W}_g\}_{g=1}^G$ denote the collection of digital precoders across all subcarriers. We aim to maximize the sum SE of all UEs in (11) by jointly optimizing digital-domain precoder \mathbf{W} , EM-domain radiation-pattern weights α_m , and spatial-domain antenna position \mathbf{p} , leading to

$$\begin{aligned} \mathcal{P}_{\text{SE}} : \quad & \max_{\{\alpha_m\}, \mathbf{W}, \mathbf{p}} R \\ \text{s.t.} \quad & \sum_{g=1}^G \|\mathbf{W}_g\|_{\text{F}}^2 \leq P_T, \\ & \|\alpha_m\|_2 = 1, \mathbf{p}_m \in \mathcal{S}_m, \forall m. \end{aligned} \quad (13)$$

where R is defined in (11) and depends on \mathbf{W} , α_m , and \mathbf{p} through the effective channel vectors $\mathbf{h}_{u,g}$ in (9). The resulting problem is highly nonconvex due to the coupled variables and the unit-norm constraints, which is challenging to be solved optimally.

III. TRI-DOMAIN ALTERNATING OPTIMIZATION: ZF-BASED BASELINE

Building upon the EM-digital alternating ZF design in [15], we extend it to SEMRA by adding a spatial-domain position-

reconfigurable block. The detailed CE-to-transmission workflow is summarized in Fig. 2, with the ZF, WMMSE, and CE components developed in Sections III-V, respectively.

A. Digital and EM-Domain Optimization

Given the current effective channels $\mathbf{h}_{u,g}$ in (9), we adopt the ZF precoder. Define the normalized channel direction and the stacked matrix as in (14).

$$\tilde{\mathbf{h}}_{u,g} \triangleq \frac{\mathbf{h}_{u,g}}{\|\mathbf{h}_{u,g}\|_2}, \quad \tilde{\mathbf{H}}_g \triangleq [\tilde{\mathbf{h}}_{1,g}, \dots, \tilde{\mathbf{h}}_{U,g}] \in \mathbb{C}^{M \times U}. \quad (14)$$

For $M \geq U$, the normalized-channel ZF precoder is computed as

$$\mathbf{W}_g = \sqrt{\frac{P_T}{G}} \frac{\tilde{\mathbf{W}}_g}{\|\tilde{\mathbf{W}}_g\|_{\text{F}}}, \quad (15)$$

where $\tilde{\mathbf{W}}_g \triangleq \tilde{\mathbf{H}}_g (\tilde{\mathbf{H}}_g^H \tilde{\mathbf{H}}_g)^{-1} \in \mathbb{C}^{M \times U}$ is the unnormalized ZF precoder built from the normalized channel directions in (14).

With \mathbf{p} and the digital precoders fixed, we update the EM-domain precoder by optimizing the block-diagonal matrix $\mathbf{\Lambda} = \text{Blkdiag}\{\alpha_1, \dots, \alpha_M\}$ under per-antenna unit-norm constraints. This is formulated on a masked oblique manifold. We define the oblique manifold

$$\mathcal{OB} \triangleq \{\mathbf{\Lambda} \in \mathbb{R}^{K \times M} : [\mathbf{\Lambda}^T \mathbf{\Lambda}]_{m,m} = 1, \forall m\}. \quad (16)$$

Let $\mathbf{M}_0 \triangleq \text{Blkdiag}\{\mathbf{1}_K, \dots, \mathbf{1}_K\} \in \mathbb{R}^{K \times M}$ and impose the structural constraint $\mathbf{\Lambda} = \mathbf{\Lambda} \odot \mathbf{M}_0$. Equivalently, the feasible EM set is $\{\mathbf{\Lambda} \in \mathcal{OB} : \mathbf{\Lambda} = \mathbf{\Lambda} \odot \mathbf{M}_0\}$. We define the cost function $f(\mathbf{\Lambda}) \triangleq -R$. The Riemannian gradient at $\mathbf{\Lambda}$ is the orthogonal projection of the Euclidean gradient $\nabla f(\mathbf{\Lambda})$ onto the tangent space, given by

$$\text{grad}f(\mathbf{\Lambda}) = \nabla f(\mathbf{\Lambda}) - \mathbf{\Lambda} \text{ddiag}(\mathbf{\Lambda}^T \nabla f(\mathbf{\Lambda})), \quad (17)$$

where $\text{ddiag}(\cdot)$ sets all off-diagonal entries of its matrix argument to zero. The retraction is column-wise normalization $\text{Retr}_{\mathbf{\Lambda}}(\gamma \mathbf{D}) \triangleq \text{normalize}(\mathbf{\Lambda} + \gamma \mathbf{D})$.

We adopt the Riemannian steepest-descent direction on this masked-oblique set, namely

$$\mathbf{D}^{(n)} = -\text{grad}f(\mathbf{\Lambda}^{(n)}), \quad (18)$$

and choose the step size $\gamma^{(n)}$ by Armijo backtracking line search on the current EM subproblem with the digital precoders fixed. The EM precoder update is then

$$\begin{aligned} \mathbf{\Lambda}^{(n+1)} &= \text{Retr}_{\mathbf{\Lambda}^{(n)}}(\gamma^{(n)} \mathbf{D}^{(n)}) \\ &= \text{normalize}(\mathbf{\Lambda}^{(n)} + \gamma^{(n)} \mathbf{D}^{(n)}). \end{aligned} \quad (19)$$

To keep the per-outer-iteration cost moderate, the EM block in both tri-domain algorithms below uses a single Armijo-controlled manifold step in each outer iteration rather than an inner loop to full convergence. Since the digital and spatial blocks are refreshed between successive EM updates, the EM descent direction is recomputed from the current gradient in every outer iteration. For compactness, variables without outer-iteration superscripts in the algorithm below denote the latest available block values within the current outer iteration. To

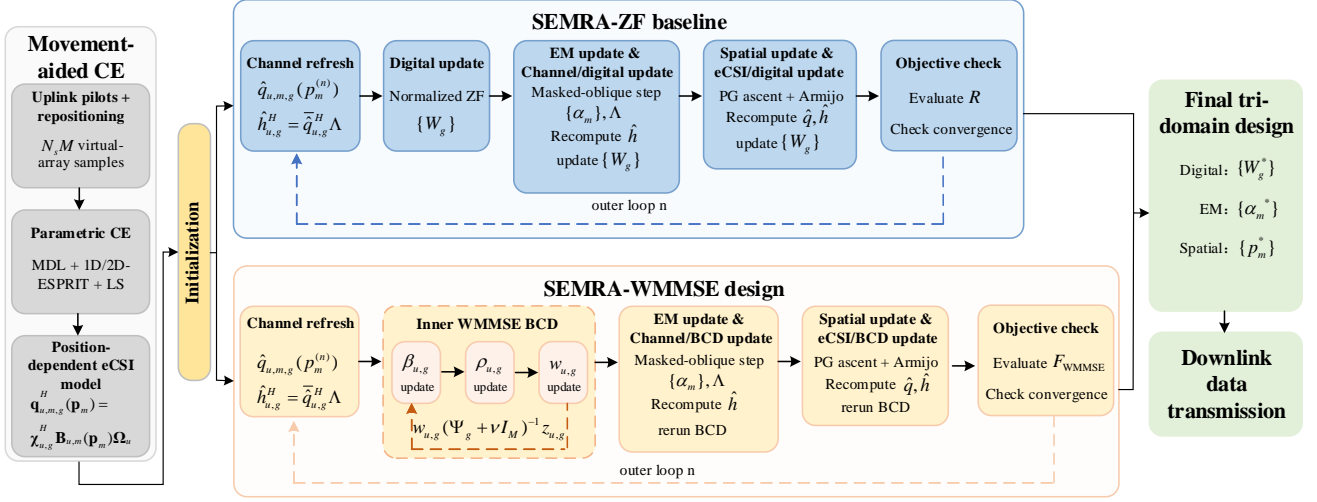


Fig. 2. Concrete workflow of the proposed SEMRA method, including movement-aided CE, position-dependent eCSI reconstruction, and ZF/WMMSE tri-domain precoding.

express the Euclidean gradient compactly, we use (9), i.e., $\mathbf{h}_{u,g}^H = \bar{\mathbf{q}}_{u,g}^H \mathbf{\Lambda}$. Let $\zeta \triangleq 1/\sigma_n^2$, and $\mathbf{W}_{\bar{u},g}$ denote the digital precoder matrix obtained from \mathbf{W}_g by removing its u -th column. The Euclidean gradient $\nabla f(\mathbf{\Lambda})$ is given by [15]

$$\nabla f(\mathbf{\Lambda}) = \left(-\sum_{g=1}^G \sum_{u=1}^U \frac{\mathbf{\Gamma}_{u,g}^{(1)} - \mathbf{\Gamma}_{u,g}^{(2)}}{\ln 2} \right) \odot \mathbf{M}_0. \quad (20)$$

The Hadamard masking enforces the block-diagonal sparsity of $\mathbf{\Lambda}$, such that each column update only acts on its corresponding K -dimensional pattern-weight block. Starting from a feasible block-diagonal initialization, the masked gradient in (20) and the retraction in (19) preserve this structure throughout the ZF-EM updates. Moreover,

$$\mathbf{\Gamma}_{u,g}^{(1)} \triangleq \frac{2\zeta \Re\{\bar{\mathbf{q}}_{u,g} \bar{\mathbf{q}}_{u,g}^H \mathbf{\Lambda} \mathbf{W}_g \mathbf{W}_g^H\}}{1 + \zeta \|\bar{\mathbf{q}}_{u,g}^H \mathbf{\Lambda} \mathbf{W}_g\|_2^2}, \quad (21)$$

$$\mathbf{\Gamma}_{u,g}^{(2)} \triangleq \frac{2\zeta \Re\{\bar{\mathbf{q}}_{u,g} \bar{\mathbf{q}}_{u,g}^H \mathbf{\Lambda} \mathbf{W}_{\bar{u},g} \mathbf{W}_{\bar{u},g}^H\}}{1 + \zeta \|\bar{\mathbf{q}}_{u,g}^H \mathbf{\Lambda} \mathbf{W}_{\bar{u},g}\|_2^2}. \quad (22)$$

B. Spatial-Domain Antenna Position Optimization

Using the available parametric eCSI model, we derive the spatial gradient of the SE objective R with respect to the conjugate channel coefficient $h_{u,m,g}^*$.

1) *Multipath Channel Decomposition*: Based on (8) and $h_{u,m,g}^* = \boldsymbol{\alpha}_m^T \mathbf{q}_{u,m,g}$, the conjugate channel admits the path-wise decomposition

$$h_{u,m,g}^* = \boldsymbol{\alpha}_m^T \boldsymbol{\Omega}_u^T \mathbf{B}_{u,m}^H \boldsymbol{\chi}_{u,g} = \sum_{i=1}^{L_u} h_{u,m,g,i}^*, \quad (23)$$

where the i -th path component is

$$h_{u,m,g,i}^* \triangleq [\boldsymbol{\Omega}_u \boldsymbol{\alpha}_m]_i [\boldsymbol{\chi}_{u,g}]_i e^{j \frac{2\pi}{\lambda} \mathbf{k}_{\text{tx},i,u}^T \mathbf{p}_m}. \quad (24)$$

Here $\mathbf{k}_{\text{tx},i,u}$ is determined by the AoD pair $(\theta_{i,u}, \phi_{i,u})$, while $\boldsymbol{\chi}_{u,g}$ absorbs the remaining position-independent factors. Therefore, the spatial update depends only on the position-dependent eCSI model, not on explicit AoA or UE-side path parameters.

2) *Sum-SE Gradient Kernel*: Define the effective coupling coefficient from the ℓ -th column of \mathbf{W}_g to the u -th UE on the g -th subcarrier as

$$c_{u,\ell,g} \triangleq \mathbf{h}_{u,g}^H \mathbf{w}_{\ell,g}, \quad \ell \in \{1, \dots, U\}. \quad (25)$$

In particular, $c_{u,u,g}$ corresponds to the desired signal term of the u -th UE, whereas $c_{u,\ell,g}$ for $\ell \neq u$ represent inter-user interference. Let $P_{u,g} \triangleq \sum_{\ell=1}^U |c_{u,\ell,g}|^2 + \sigma_n^2$ and $\mathcal{I}_{u,g} \triangleq \sum_{\ell \neq u}^U |c_{u,\ell,g}|^2 + \sigma_n^2$, so that $\text{SINR}_{u,g} = |c_{u,u,g}|^2 / \mathcal{I}_{u,g}$, $1 + \text{SINR}_{u,g} = P_{u,g} / \mathcal{I}_{u,g}$ and $r_{u,g} = \log_2(P_{u,g}) - \log_2(\mathcal{I}_{u,g})$. Moreover, $\frac{\partial |c_{u,\ell,g}|^2}{\partial h_{u,m,g}^*} = c_{u,\ell,g}^* w_{\ell,m,g}$ with $w_{\ell,m,g} = [\mathbf{w}_{\ell,g}]_m$. Applying the chain rule yields the sensitivity of R with respect to $h_{u,m,g}^*$ as

$$\xi_{u,m,g}^{(R)} \triangleq \frac{\partial R}{\partial h_{u,m,g}^*} = \frac{1}{\ln 2 \cdot P_{u,g}} \left(c_{u,u,g}^* w_{u,m,g} - \text{SINR}_{u,g} \sum_{\ell \neq u}^U c_{u,\ell,g}^* w_{\ell,m,g} \right). \quad (26)$$

3) *Spatial Gradient Assembly and Projection*: From (24), differentiating the conjugate path component $h_{u,m,g,i}^*$ with respect to \mathbf{p}_m yields $\frac{\partial h_{u,m,g,i}^*}{\partial \mathbf{p}_m} = j \frac{2\pi}{\lambda} \mathbf{k}_{\text{tx},i,u} h_{u,m,g,i}^*$. Using Wirtinger calculus and noting that $\mathbf{p}_m \in \mathbb{R}^3$ and R is real-valued, the real gradient satisfies $\nabla_{\mathbf{p}_m} R = 2\Re\{\sum_{u,g} \frac{\partial R}{\partial h^*} \frac{\partial h^*}{\partial \mathbf{p}_m}\}$. Exploiting $2\Re\{jz\} = -2\Im\{z\}$, we obtain

$$\nabla_{\mathbf{p}_m} R = -\frac{4\pi}{\lambda} \Im \left\{ \sum_{g=1}^G \sum_{u=1}^U \xi_{u,m,g}^{(R)} \sum_{i=1}^{L_u} h_{u,m,g,i}^* \mathbf{k}_{\text{tx},i,u} \right\}. \quad (27)$$

The ZF spatial block updates the antenna positions by the projected gradient ascent step

$$\mathbf{p}_m^{(n+1)} = \Pi_{\mathcal{S}_m} \left(\mathbf{p}_m^{(n)} + \eta_p \nabla_{\mathbf{p}_m} R \right), \quad (28)$$

where $\eta_p > 0$ is the step size determined by the Armijo backtracking line search on R with $\mathbf{\Lambda}$ and the digital precoders fixed. The projection $\Pi_{\mathcal{S}_m}(\cdot)$ maps the updated point onto

the feasible region (12) via component-wise clipping. Specifically, $[\Pi_{\mathcal{S}_m}(\mathbf{x})]_1 = 0$ enforces the planar constraint, while $[\Pi_{\mathcal{S}_m}(\mathbf{x})]_k = \min(\max([\mathbf{x}]_k, [\bar{\mathbf{p}}_m]_k - D_{\max}), [\bar{\mathbf{p}}_m]_k + D_{\max})$ for $k \in \{2, 3\}$ confines the displacement to the box region. The inner loop repeats the antenna-wise updates until the spatial subproblem subconverges, and the overall ZF-based tri-domain procedure is summarized in Algorithm 1.

IV. TRI-DOMAIN ALTERNATING OPTIMIZATION: WMMSE-BASED DESIGN

Beyond the ZF-based baseline algorithm introduced in Section III, we develop a tri-domain WMMSE-based algorithm to solve (13) under a global total-power constraint in this section. Specifically, the WMMSE reformulation yields closed-form auxiliary and digital updates, while the EM block uses an Armijo-controlled manifold step and the spatial block is handled by an inner BCD loop with projected-gradient position updates.

A. WMMSE Problem Transformation

1) *Signal Estimation and Mean Square Error:* For each user-subcarrier pair, we introduce a scalar receive equalizer $\beta_{u,g} \in \mathbb{C}$ and the estimated symbol $\hat{s}_{u,g} \triangleq \beta_{u,g}^* y_{u,g}$. The

mean square error (MSE) $\varepsilon_{u,g} \triangleq \mathbb{E}\{|\beta_{u,g}^* y_{u,g} - s_{u,g}|^2\}$ then expands via (1) as

$$\varepsilon_{u,g} = \underbrace{|\beta_{u,g}^* \mathbf{h}_{u,g}^H \mathbf{w}_{u,g} - 1|^2}_{\text{signal distortion}} + \underbrace{\sum_{\substack{\ell=1 \\ \ell \neq u}}^U |\beta_{u,g}^* \mathbf{h}_{u,g}^H \mathbf{w}_{\ell,g}|^2}_{\text{multiuser interference}} + \underbrace{\sigma_n^2 |\beta_{u,g}|^2}_{\text{noise amplification}}, \quad (29)$$

where $\mathbf{h}_{u,g}$ is defined in (9) and its dependence on \mathbf{p} and $\boldsymbol{\alpha}_m$ is omitted for notational brevity.

2) *WMMSE Equivalence:* By the WMMSE equivalence [33], the sum-SE maximization problem (13) can be equivalently reformulated by introducing auxiliary minimum mean square error (MMSE) receivers $\beta_{u,g}$ and positive MSE weights $\rho_{u,g}$ for each user-subcarrier pair, yielding

$$\begin{aligned} \mathcal{P}_{\text{WMMSE}} : \quad & \min_{\mathcal{V}} F_{\text{WMMSE}} \\ \text{s.t.} \quad & \sum_{g=1}^G \sum_{u=1}^U \|\mathbf{w}_{u,g}\|_2^2 \leq P_T, \\ & \|\boldsymbol{\alpha}_m\|_2 = 1, \boldsymbol{\alpha}_m \in \mathbb{R}^K, \forall m, \\ & \mathbf{p}_m \in \mathcal{S}_m, \forall m, \rho_{u,g} > 0, \forall u, g, \end{aligned} \quad (30)$$

where $\mathcal{V} \triangleq \{\{\mathbf{w}_{u,g}\}, \{\boldsymbol{\alpha}_m\}, \{\mathbf{p}_m\}, \{\beta_{u,g}\}, \{\rho_{u,g}\}\}$ denotes the collection of all optimization variables, and the WMMSE objective function is defined as

$$F_{\text{WMMSE}} \triangleq \sum_{g=1}^G \sum_{u=1}^U (\rho_{u,g} \varepsilon_{u,g} - \ln \rho_{u,g}). \quad (31)$$

For fixed \mathbf{W} , $\boldsymbol{\alpha}_m$, and \mathbf{p} , optimizing the auxiliary variables $\beta_{u,g}$ and $\rho_{u,g}$ yields $\min_{\{\beta_{u,g}\}, \{\rho_{u,g} > 0\}} F_{\text{WMMSE}} = UG - (\ln 2) R$. Hence, after eliminating the auxiliary variables, minimizing F_{WMMSE} over the remaining design variables is equivalent to maximizing R in (11). The reformulation also yields closed-form updates for $\beta_{u,g}$, $\rho_{u,g}$, and $\mathbf{w}_{u,g}$, whereas the EM- and spatial-domain blocks remain nonconvex and are handled in Sections IV-C and IV-D.

Substituting (29) into (31) and expanding, the WMMSE objective becomes

$$\begin{aligned} F_{\text{WMMSE}} = \sum_{g=1}^G \sum_{u=1}^U & \left[\rho_{u,g} \left(|\beta_{u,g}^* \mathbf{h}_{u,g}^H \mathbf{w}_{u,g} - 1|^2 \right. \right. \\ & \left. \left. + \sum_{\substack{\ell=1 \\ \ell \neq u}}^U |\beta_{u,g}^* \mathbf{h}_{u,g}^H \mathbf{w}_{\ell,g}|^2 + \sigma_n^2 |\beta_{u,g}|^2 \right) - \ln \rho_{u,g} \right]. \end{aligned} \quad (32)$$

B. Digital Precoding and Auxiliary Variable Optimization

With antenna positions \mathbf{p} and EM-domain precoders $\boldsymbol{\alpha}_m$ fixed, the first block minimizes F_{WMMSE} over the auxiliary variables $\beta_{u,g}$, $\rho_{u,g}$, and the digital precoders $\mathbf{w}_{u,g}$ via BCD. Each subproblem is convex in its own variable block and therefore admits a closed-form update.

Algorithm 1: ZF-based tri-domain alternating optimization

Input: Position-dependent eCSI model; feasible sets $\{\mathcal{S}_m\}_{m=1}^M$; power budget P_T ; stopping parameters (N_{\max}, ϵ) ; Armijo line-search parameters.
Output: Final design $\{\mathbf{W}_g\}_{g=1}^G$, $\{\boldsymbol{\alpha}_m\}_{m=1}^M$, and $\{\mathbf{p}_m\}_{m=1}^M$.

- 1 Initialization: set $\mathbf{p}_m^{(0)} = \bar{\mathbf{p}}_m$ and choose feasible unit-norm $\boldsymbol{\alpha}_m^{(0)}$, $\forall m$;
- 2 Build $\mathbf{A}^{(0)}$ and the initial effective channels via (9);
- 3 Digital initialization: compute $\{\mathbf{W}_g^{(0)}\}_{g=1}^G$ via (14)-(15) and evaluate $R^{(0)}$ via (11);
- 4 **for** $n = 0$ **to** $N_{\max} - 1$ **do**
- 5 Channel update: evaluate $\{\mathbf{q}_{u,m,g}\}_{u,m,g=1}^{U,M,G}$ at $\{\mathbf{p}_m^{(n)}\}$ and build $\{\mathbf{h}_{u,g}\}_{u,g=1}^{U,G}$ via (9);
- 6 Digital update: compute $\{\mathbf{W}_g\}$ by normalized ZF via (14)-(15);
- 7 EM update: compute the Riemannian descent direction for the current EM subproblem via (18), take one Armijo-controlled masked-oblique update via (19), and extract $\{\boldsymbol{\alpha}_m^{(n+1)}\}$;
- 8 EM refresh: rebuild $\{\mathbf{h}_{u,g}\}$ with the updated EM block and update $\{\mathbf{W}_g\}$;
- 9 Position update: run the inner spatial BCD loop, where antenna positions are cyclically updated by Armijo-controlled projected-gradient ascent steps via (27) and (28), to obtain $\{\mathbf{p}_m^{(n+1)}\}$;
- 10 Position refresh: reevaluate $\{\mathbf{q}_{u,m,g}\}$ at $\{\mathbf{p}_m^{(n+1)}\}$, rebuild $\{\mathbf{h}_{u,g}\}$, and update $\{\mathbf{W}_g\}$;
- 11 Objective update: compute $R^{(n+1)}$ via (11);
- 12 **if** $\frac{|R^{(n+1)} - R^{(n)}|}{\max\{1, |R^{(n)}|\}} \leq \epsilon$ **then**
- 13 **break**;
- 14 **end**
- 15 **end**
- 16 **return** final design $\{\mathbf{W}_g\}_{g=1}^G$, $\{\boldsymbol{\alpha}_m\}_{m=1}^M$, and $\{\mathbf{p}_m\}_{m=1}^M$;

1) *Optimal Receive Equalizer Update:* We first optimize the scalar receive equalizer $\beta_{u,g}$ for each user-subcarrier pair while keeping $\mathbf{w}_{u,g}$ and $\rho_{u,g}$ fixed. Setting $\partial \varepsilon_{u,g} / \partial \beta_{u,g}^* = 0$ in (29) yields the MMSE receiver given by

$$\beta_{u,g}^* = \frac{\mathbf{h}_{u,g}^H \mathbf{w}_{u,g}}{\sum_{\ell=1}^U |\mathbf{h}_{u,g}^H \mathbf{w}_{\ell,g}|^2 + \sigma_n^2}. \quad (33)$$

2) *Optimal MSE Weight Update:* Setting $\partial(\rho_{u,g} \varepsilon_{u,g} - \ln \rho_{u,g}) / \partial \rho_{u,g} = 0$ gives $\rho_{u,g}^* = 1 / \varepsilon_{u,g}$. When the optimal equalizer (33) is substituted, the minimum MSE reduces to $\varepsilon_{u,g}^{\min} = (1 + \text{SINR}_{u,g})^{-1}$ by the orthogonality principle, yielding

$$\rho_{u,g}^* = 1 + \text{SINR}_{u,g}. \quad (34)$$

3) *Optimal Digital Precoder Update:* Finally, we optimize the digital precoders $\mathbf{w}_{u,g}$ subject to the total power constraint. Removing the terms independent of $\mathbf{w}_{u,g}$ from (32), the subproblem becomes the following quadratically constrained quadratic program (QCQP)

$$\begin{aligned} \min_{\{\mathbf{w}_{u,g}\}} \quad & \sum_{g=1}^G \sum_{u=1}^U \rho_{u,g} \varepsilon_{u,g} \\ \text{s.t.} \quad & \sum_{g=1}^G \sum_{u=1}^U \|\mathbf{w}_{u,g}\|_2^2 \leq P_T. \end{aligned} \quad (35)$$

To decouple the precoders across users, we first expand the weighted MSE. Interchanging the summation order over users u and interferers ℓ , the objective function can be rewritten as (with constants independent of $\mathbf{w}_{u,g}$ omitted)

$$J(\{\mathbf{w}_{u,g}\}) = \sum_{g=1}^G \sum_{u=1}^U (\mathbf{w}_{u,g}^H \Psi_g \mathbf{w}_{u,g} - 2\Re\{\mathbf{w}_{u,g}^H \mathbf{z}_{u,g}\}), \quad (36)$$

where we define the weighted channel covariance matrix as $\Psi_g \triangleq \sum_{\ell=1}^U \rho_{\ell,g} |\beta_{\ell,g}|^2 \mathbf{h}_{\ell,g} \mathbf{h}_{\ell,g}^H \in \mathbb{C}^{M \times M}$ and the equivalent target vector as $\mathbf{z}_{u,g} \triangleq \rho_{u,g} \beta_{u,g} \mathbf{h}_{u,g} \in \mathbb{C}^M$.

We solve (35) via the Lagrangian method. Let $\nu \geq 0$ denote the dual variable associated with the power constraint. The Karush-Kuhn-Tucker (KKT) stationarity condition $\partial \mathcal{L} / \partial \mathbf{w}_{u,g}^* = \mathbf{0}$ yields $(\Psi_g + \nu \mathbf{I}_M) \mathbf{w}_{u,g} = \mathbf{z}_{u,g}$. Since $\Psi_g \succeq \mathbf{0}$, the matrix $\Psi_g + \nu \mathbf{I}_M$ is positive definite for any $\nu > 0$, and the optimal precoder admits the closed-form solution

$$\mathbf{w}_{u,g}^*(\nu) = (\Psi_g + \nu \mathbf{I}_M)^{-1} \mathbf{z}_{u,g}. \quad (37)$$

Since Ψ_g has rank at most U , it is singular whenever $U < M$. However, $\mathbf{z}_{u,g} = \rho_{u,g} \beta_{u,g} \mathbf{h}_{u,g}$ is collinear with $\mathbf{h}_{u,g}$, and the u -th term of Ψ_g is scaled by $\rho_{u,g} |\beta_{u,g}|^2$, so $\mathbf{z}_{u,g}$ lies in the column space range(Ψ_g) of Ψ_g whenever $\beta_{u,g} \neq 0$, while the case $\beta_{u,g} = 0$ gives $\mathbf{z}_{u,g} = \mathbf{0}$ trivially. Therefore, the limit $\lim_{\nu \rightarrow 0^+} \mathbf{w}_{u,g}^*(\nu) = \Psi_g^\dagger \mathbf{z}_{u,g}$ is well-defined, and we define $\mathbf{w}_{u,g}^*(0) \triangleq \Psi_g^\dagger \mathbf{z}_{u,g}$. The optimal Lagrange multiplier ν^* is determined by complementary slackness. If $\sum_{g,u} \|\mathbf{w}_{u,g}^*(0)\|_2^2 \leq P_T$, then $\nu^* = 0$ and the power constraint is inactive, otherwise, $\nu^* > 0$ is the unique root of $\sum_{g,u} \|\mathbf{w}_{u,g}^*(\nu)\|_2^2 = P_T$, which can be found by bisection since the left-hand side is monotonically decreasing in ν . Unlike the normalized ZF baseline in Section III, this

digital update enforces only the global total-power constraint and can therefore redistribute digital power across users and subcarriers.

C. EM-Domain Radiation Pattern Optimization

With \mathbf{W} , \mathbf{p} , $\beta_{u,g}$, and $\rho_{u,g}$ fixed, we optimize the EM-domain weights α_m , or equivalently the block-diagonal matrix $\Lambda = \text{Blkdiag}\{\alpha_1, \dots, \alpha_M\} \in \mathbb{R}^{KM \times M}$. As in Section III-A, we reuse the masked-oblique manifold framework, and only the objective and its Euclidean gradient change.

1) *Subproblem Formulation:* With \mathbf{W} , \mathbf{p} , $\beta_{u,g}$, and $\rho_{u,g}$ fixed, the EM-domain subproblem is

$$\begin{aligned} \min_{\Lambda \in \mathcal{OB}} \quad & \mathfrak{f}_{\text{EM}}(\Lambda) \triangleq \sum_{g=1}^G \sum_{u=1}^U \rho_{u,g} \varepsilon_{u,g} \\ \text{s.t.} \quad & \Lambda = \Lambda \odot \mathbf{M}_0, \end{aligned} \quad (38)$$

where $\varepsilon_{u,g}$ is given in (29) and \mathbf{M}_0 is the block-diagonal mask from Section III-A. Since the weights $\rho_{u,g}$ are fixed, the term $-\sum_{g,u} \ln \rho_{u,g}$ in (31) is an additive constant and is omitted.

2) *Euclidean Gradient of the EM Objective:* From (9), the effective channel satisfies $\mathbf{h}_{u,g}^H = \bar{\mathbf{q}}_{u,g}^H \Lambda$. Let $c_{u,\ell,g} \triangleq \mathbf{h}_{u,g}^H \mathbf{w}_{\ell,g}$ be defined as in (25). We define the WMMSE MSE-residual kernel as

$$\begin{aligned} \xi_{u,m,g}^{(\varepsilon)} & \triangleq \frac{\partial(\rho_{u,g} \varepsilon_{u,g})}{\partial h_{u,m,g}^*} \\ & = \rho_{u,g} \left(|\beta_{u,g}|^2 \sum_{\ell=1}^U c_{u,\ell,g}^* w_{\ell,m,g} - \beta_{u,g}^* w_{u,m,g} \right), \end{aligned} \quad (39)$$

where $w_{\ell,m,g} = [\mathbf{w}_{\ell,g}]_m$. Stacking the kernel into $\xi_{u,g}^{(\varepsilon)} \triangleq [\xi_{u,1,g}^{(\varepsilon)}, \dots, \xi_{u,M,g}^{(\varepsilon)}]^T \in \mathbb{C}^M$ and noting that Λ is real-valued, the chain rule yields

$$\nabla \mathfrak{f}_{\text{EM}}(\Lambda) = \left(2\Re \left\{ \sum_{g=1}^G \sum_{u=1}^U \mathbf{q}_{u,g} (\xi_{u,g}^{(\varepsilon)})^T \right\} \right) \odot \mathbf{M}_0. \quad (40)$$

3) *Masked-Oblique Manifold Update:* With the Euclidean gradient in (40), we reuse the one-step masked-oblique update (18)-(19) with $\mathfrak{f}(\cdot)$ replaced by $\mathfrak{f}_{\text{EM}}(\cdot)$ in (38). As in Section III-A, each outer iteration recomputes the EM descent direction from the current gradient, takes one Armijo-controlled manifold step, extracts the updated per-antenna weights α_m from the diagonal blocks of Λ , and then performs the subsequent digital refresh used in Algorithm 2. To keep the outer-loop complexity manageable, the algorithm uses only this one manifold step per outer iteration rather than an inner EM loop. The initialization uses a maximum-ratio transmission (MRT) digital precoder followed by one global normalization to satisfy the total-power constraint at $n = 0$.

D. Spatial-Domain Antenna Position Optimization

With \mathbf{W} , α_m , $\beta_{u,g}$, and $\rho_{u,g}$ fixed, the final block updates $\mathbf{p} \triangleq [\mathbf{p}_1^T, \dots, \mathbf{p}_M^T]^T$ by minimizing $\mathfrak{f}_{\text{pos}}(\mathbf{p}) \triangleq \sum_{g,u} \rho_{u,g} \varepsilon_{u,g}$ subject to $\mathbf{p}_m \in \mathcal{S}_m$, where the constant $-\sum_{g,u} \ln \rho_{u,g}$ is omitted as in (38).

Algorithm 2: WMMSE-based tri-domain alternating optimization

Input: Position-dependent eCSI model; feasible sets $\{\mathcal{S}_m\}_{m=1}^M$; power budget P_T ; stopping parameters (N_{\max}, ϵ) ; Armijo line-search parameters.

Output: Final design $\{\mathbf{W}_g\}_{g=1}^G$, $\{\alpha_m\}_{m=1}^M$, and $\{\mathbf{p}_m\}_{m=1}^M$.

- 1 Initialization: set $\mathbf{p}_m^{(0)} = \bar{\mathbf{p}}_m$ and choose feasible unit-norm $\alpha_m^{(0)}$, $\forall m$;
- 2 Build $\mathbf{A}^{(0)}$ and the initial effective channels via (9);
- 3 Digital initialization: initialize $\{\mathbf{W}_g^{(0)}\}_{g=1}^G$ by MRT and scale them to satisfy $\sum_{g=1}^G \|\mathbf{W}_g^{(0)}\|_{\text{F}}^2 = P_T$; update $\beta_{u,g}^{(0)}$ and $\rho_{u,g}^{(0)}$ via (33)-(34); evaluate $F_{\text{WMMSE}}^{(0)}$ via (31);
- 4 **for** $n = 0$ to $N_{\max} - 1$ **do**
 - 5 Channel update: evaluate $\{\mathbf{q}_{u,m,g}\}_{u,m,g=1}^{U,M,G}$ at $\{\mathbf{p}_m^{(n)}\}$ and build $\{\mathbf{h}_{u,g}\}_{u,g=1}^{U,G}$ via (9);
 - 6 Digital-WMMSE update: cyclically update $\beta_{u,g}$ and $\rho_{u,g}$ via (33)-(34) and $\{\mathbf{W}_g\}$ via (37) (with ν^* determined by the inactive-constraint check and bisection when needed) until F_{WMMSE} subconverges;
 - 7 EM update: compute the Riemannian descent direction for the current EM subproblem via (18), take one Armijo-controlled masked-oblique update via (19), and extract $\{\alpha_m^{(n+1)}\}$;
 - 8 Digital refresh: rebuild $\{\mathbf{h}_{u,g}\}$ with the updated EM block and rerun the inner BCD on $(\beta_{u,g}, \rho_{u,g}, \mathbf{w}_{u,g})$ until F_{WMMSE} subconverges;
 - 9 Position update: run the inner spatial BCD loop, where antenna positions are cyclically updated by Armijo-controlled projected-gradient steps via (41) and (42), to obtain $\{\mathbf{p}_m^{(n+1)}\}$;
 - 10 Objective update: reevaluate $\{\mathbf{q}_{u,m,g}\}$ and $\{\mathbf{h}_{u,g}\}$ at $\{\mathbf{p}_m^{(n+1)}\}$, rerun the inner BCD on $(\beta_{u,g}, \rho_{u,g}, \mathbf{w}_{u,g})$ until F_{WMMSE} subconverges, and evaluate $F_{\text{WMMSE}}^{(n+1)}$;
 - 11 **if** $\frac{|F_{\text{WMMSE}}^{(n+1)} - F_{\text{WMMSE}}^{(n)}|}{\max\{1, |F_{\text{WMMSE}}^{(n)}|\}} \leq \epsilon$ **then**
 - 12 | **break**;
 - 13 **end**
- 14 **end**
- 15 **return** final design $\{\mathbf{W}_g\}_{g=1}^G$, $\{\alpha_m\}_{m=1}^M$, and $\{\mathbf{p}_m\}_{m=1}^M$;

1) *Spatial Gradient:* Repeating the derivation of Section III-B, i.e., using the same decomposition in (23)-(24) together with $\partial h_{u,m,g,i}^* / \partial \mathbf{p}_m = j \frac{2\pi}{\lambda} \mathbf{k}_{\text{tx},i,u} h_{u,m,g,i}^*$, but replacing $\xi_{u,m,g}^{(R)}$ by $\xi_{u,m,g}^{(\varepsilon)}$ from (39), gives

$$\mathbf{g}_m^{\text{pos}} \triangleq \nabla_{\mathbf{p}_m} f_{\text{pos}}(\mathbf{p})$$

$$= -\frac{4\pi}{\lambda} \Im \left\{ \sum_{g=1}^G \sum_{u=1}^U \xi_{u,m,g}^{(\varepsilon)} \sum_{i=1}^{L_u} h_{u,m,g,i}^* \mathbf{k}_{\text{tx},i,u} \right\}. \quad (41)$$

2) *Position Update with Projection:* The spatial block is optimized by an inner BCD loop over antenna positions. Within this loop, each antenna position is updated by a projected gradient descent (PGD) step according to

$$\mathbf{p}_m^{(n+1)} = \Pi_{\mathcal{S}_m} \left(\mathbf{p}_m^{(n)} - \eta_p \mathbf{g}_m^{\text{pos}} \right), \quad (42)$$

which is the WMMSE counterpart of (28). As in Section III-B, each PGD step uses the same feasible-set projection and Armijo line search, so all intermediate antenna positions remain feasible. The BCD loop repeats these antenna-wise updates until the spatial subproblem subconverges before returning $\{\mathbf{p}_m^{(n+1)}\}$ to the outer tri-domain iteration.

V. LOW-OVERHEAD MOVEMENT-AIDED CE SCHEME

The tri-domain optimization developed in Sections III-IV requires a position-dependent eCSI model so that $\mathbf{q}_{u,m,g}$ can

be evaluated for all users, antennas, and subcarriers at the current antenna positions. In the fixed-position EMRA baseline following [15], the same parametric pipeline is applied on the reference array. One-dimensional (1D) ESPRIT is used for delay estimation, followed by two-dimensional (2D) ESPRIT for AoD estimation. Because the array geometry remains fixed, the angular resolution is fundamentally limited by the M physical spatial samples. For a moderate array size, AoD estimation accuracy degrades and the resulting eCSI quality deteriorates.

We overcome this limitation by exploiting the spatial reconfigurability of SEMRA. At the uplink CE stage, all M antennas are simultaneously repositioned over N_s successive pilot slots, with each antenna visiting N_s prescribed observation positions to collectively form a densified virtual array with $N_s M$ spatial samples while using only M physical antennas. The proposed scheme adopts a parametric estimation framework in which the multipath delays, AoD angles, and an equivalent channel gain vector, all independent of the BS antenna positions, are extracted as intermediate parameters. This position-invariant parameterization decouples CE from the subsequent data-transmission design. During CE, the antennas move to observation positions for high-resolution parameter extraction, and the eCSI at the optimized positions is then assembled directly from the estimated parameters without additional pilot overhead. Since uplink-downlink channel reciprocity holds in TDD, the BS-side angles estimated during the uplink CE phase coincide with the downlink AoD parameters $(\theta_{i,u}, \phi_{i,u})$ defined in Section II-B, and we retain the downlink notation throughout this section.

A. Virtual Array Construction

1) *Observation Position Design:* For this specific CE procedure, we assume equal inter-element spacings $d \triangleq d_y = d_z$ and define $d_{\min} \triangleq d/4$. For each BS antenna m , the reference position $\bar{\mathbf{p}}_m$ serves as the center around which $N_s = 4$ observation positions are defined as

$$\mathbf{p}_m^{(s)} = \bar{\mathbf{p}}_m + \Delta_s, \quad s = 1, \dots, N_s, \quad (43)$$

with the displacement vectors

$$\Delta_s = \begin{bmatrix} 0 \\ \psi_{y,s} d_{\min} \\ \psi_{z,s} d_{\min} \end{bmatrix}, \quad (\psi_{y,s}, \psi_{z,s}) \in \left\{ \begin{array}{l} (+1, +1), (+1, -1), \\ (-1, +1), (-1, -1) \end{array} \right\}, \quad (44)$$

for $s = 1, \dots, 4$, respectively. Thus, each observation position is offset from $\bar{\mathbf{p}}_m$ by $\pm d_{\min}$ along both the y - and z -axes. The design requires $D_{\max} \geq d_{\min} = d/4$ so that all observation positions lie within the feasible region (12). This is compatible with the non-overlapping condition $d \geq 2D_{\max} + D_{\text{sep}}$ in Section II-D. Both constraints are jointly satisfiable whenever $D_{\text{sep}} < d/2$.

A fixed preselected CE-stage real-valued pattern coefficient vector $\alpha_{\text{ce}} \in \mathbb{R}^K$ with $\|\alpha_{\text{ce}}\|_2 = 1$ is used throughout, so no CE-pattern optimization is performed, and the fixed pattern preserves the virtual-array coherence used next. We assume that the channel remains quasi-static at the CE stage and that the antenna repositioning latency is negligible compared with the channel coherence time.

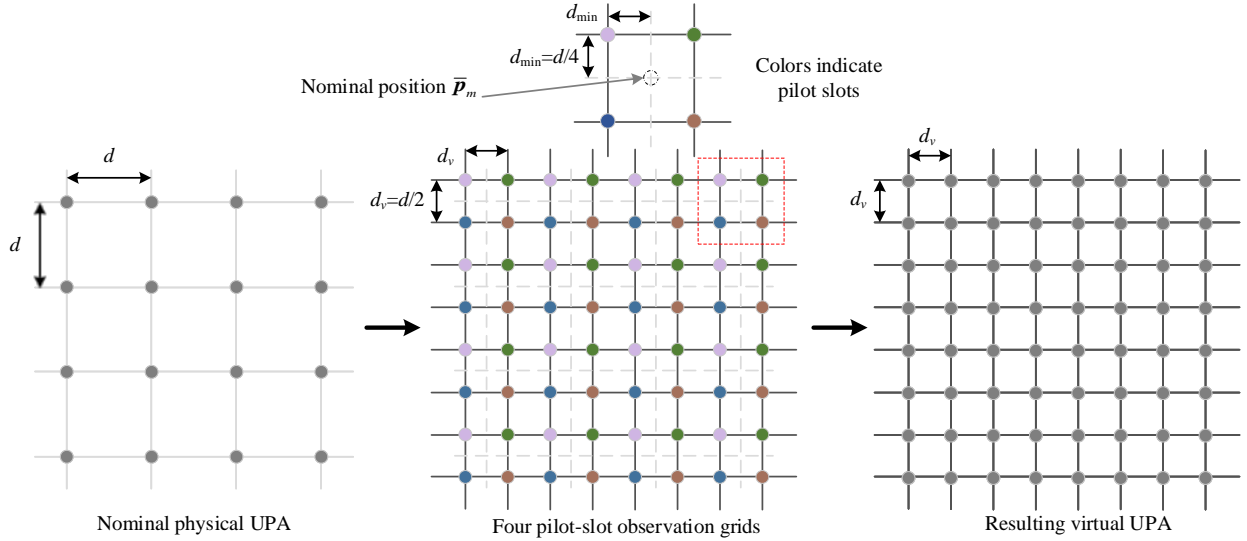


Fig. 3. Virtual-array construction for movement-aided CE. From an $M_y \times M_z$ reference UPA with spacing d , the observation positions visited over four pilot slots interleave to form a uniform $2M_y \times 2M_z$ virtual UPA with spacing $d_v = d/2$. The illustration is shown for $M_y = M_z = 4$.

2) *Virtual UPA Formation*: The resulting virtual-array geometry is illustrated in Fig. 3. Across N_s slots, the M antennas occupy $N_s M = 4M$ distinct spatial positions. Within a single antenna m , its four observation positions occupy the corners of a 2×2 arrangement centered at $\bar{\mathbf{p}}_m$ with nearest-neighbor distance $2d_{\min}$. Between two neighboring antennas whose reference positions are spaced by d , the closest observation positions from the respective four-point arrangements are separated by $d - 2d_{\min}$. The choice $d_{\min} = d/4$ yields $2d_{\min} = d - 2d_{\min} = d/2$, so both intra-antenna and inter-antenna nearest-neighbor distances equal $d/2$. The $4M$ positions therefore constitute a uniform $2M_y \times 2M_z$ virtual UPA with element spacing $d_v \triangleq d/2$. The resulting virtual aperture is $(2M_y - 1)d_v \times (2M_z - 1)d_v = (M_y - \frac{1}{2})d \times (M_z - \frac{1}{2})d$, exceeding the original $(M_y - 1)d \times (M_z - 1)d$ by $\frac{1}{2}d$ along each dimension. Meanwhile, the number of spatial observation points increases from M to $4M$, and the inter-element spacing is halved along both dimensions. This denser spatial sampling and the modest aperture enlargement mainly benefit the 2D-ESPRIT stage, which estimates AoD from the spatial covariance of the observations. The delay stage remains dominated by frequency-domain shift invariance and is therefore much less sensitive to the movement-induced spatial densification.

B. Parametric Channel Estimation

The discussion assumes the standard subspace-identifiability conditions for the minimum description length (MDL)/ESPRIT pipeline, under which the delay and spatial steering structures are resolvable for the chosen pilot and virtual-array dimensions, and we focus on a generic UE u .

1) *Delay Estimation and sCSI Recovery*: In each pilot slot s , UE u transmits pilots on a dedicated subset $\mathcal{G}_u = \{g_{u,1}, \dots, g_{u,J}\}$ of J uniformly spaced subcarriers ($J \leq G/U$), where the subsets of different users are disjoint to avoid

mutual interference. The signal received at BS antenna m on pilot subcarrier g_j is

$$y_{u,m,g_j}^{(s)} = (h_{u,m,g_j}^{(s)})^* s_{u,g_j} + n_{u,m,g_j}^{(s)}, \quad (45)$$

where s_{u,g_j} is the known pilot symbol and $n_{u,m,g_j}^{(s)}$ denotes receiver noise. Dividing by the pilot gives the effective observation $\hat{y}_{u,m,g_j}^{(s)} = (h_{u,m,g_j}^{(s)})^* + \tilde{n}_{u,m,g_j}^{(s)}$. Under the downlink convention used here, reciprocity gives the uplink scalar coefficient as $(h_{u,m,g_j}^{(s)})^*$. The frequency-domain observations from all $N_s M$ observation positions are divided by the known pilot symbols and stacked column-wise into a data matrix $\mathbf{Y}_d \in \mathbb{C}^{J \times N_s M}$, where each column corresponds to a distinct observation position. Because the multipath channel (2) is a sum of complex exponentials across frequency, \mathbf{Y}_d can be written as $\mathbf{Y}_d = \mathbf{E}_d \mathbf{X}_d + \mathbf{N}_d$. Here, $\mathbf{E}_d \in \mathbb{C}^{J \times L_u}$ is a Vandermonde-structured delay steering matrix, $\mathbf{X}_d \in \mathbb{C}^{L_u \times N_s M}$ collects the equivalent path gains across observation positions, and \mathbf{N}_d is the corresponding noise matrix.

The number of multipath components L_u is estimated, rather than assumed known a priori, by applying the MDL criterion to the eigenvalues of the sample covariance matrix $\mathbf{Y}_d \mathbf{Y}_d^H \in \mathbb{C}^{J \times J}$ [34], yielding the model-order estimate \hat{L}_u . The estimated order \hat{L}_u is then used in the subsequent 1D-ESPRIT stage.

With \hat{L}_u determined, the 1D-ESPRIT algorithm extracts the multipath delays $\{\hat{\tau}_{i,u}\}_{i=1}^{\hat{L}_u}$ from the shift-invariance structure of \mathbf{E}_d . The full-band sCSI $\hat{h}_{u,m,g}^{(s)}$ is then recovered by delay-domain LS fitting at the CE observation positions, i.e., the $M_y \times M_z$ reference-array positions for EMRA and the $N_s M$ positions of the $2M_y \times 2M_z$ virtual UPA for SEMRA.

2) *AoD Estimation on the Virtual Array*: At each observation position $\mathbf{p}_m^{(s)}$, the spatial-domain channel on subcarrier g can be expressed as

$$h_{u,m,g}^{(s)} = \sum_{i=1}^{\hat{L}_u} \hat{x}_{i,u,g} e^{-j \frac{2\pi}{\lambda} \mathbf{k}_{\text{tx},i,u}^T \mathbf{p}_m^{(s)}}, \quad (46)$$

where $\hat{x}_{i,u,g} \triangleq x_{i,u,g} f_{\text{rx},u}(\vartheta_{i,u}, \varphi_{i,u}) (\boldsymbol{\alpha}_{\text{ce}}^T \boldsymbol{\omega}_{i,u}) e^{-j \frac{2\pi}{\lambda} \mathbf{k}_{\text{rx},i,u}^T \mathbf{r}_u}$ with $\boldsymbol{\omega}_{i,u} \triangleq [\omega_1(\theta_{i,u}, \phi_{i,u}), \dots, \omega_K(\theta_{i,u}, \phi_{i,u})]^T$. Because the radiation pattern $\boldsymbol{\alpha}_{\text{ce}}$ is held fixed across all slots and antennas, the composite gain $\hat{x}_{i,u,g}$ does not depend on the antenna index m or the slot index s . The $4M$ spatial observations therefore exhibit the canonical steering-vector structure of a $2M_y \times 2M_z$ UPA with inter-element spacing d_v , so the standard 2D-ESPRIT procedure [18] can be applied after the re-indexing and spatial-smoothing steps described next. Concretely, the recovered sCSI values $\{\hat{h}_{u,m,g}^{(s)}\}$ at the virtual-array positions are arranged into a data matrix of size $N_s M \times G$, where rows index the $N_s M$ virtual-array positions and columns index the G subcarriers. Each subcarrier contributes one snapshot of the same spatial steering structure, with a different composite gain $\hat{x}_{i,u,g}$, and the 2D-ESPRIT algorithm estimates the spatial frequencies $\{\hat{\mu}_{i,u}, \hat{\nu}_{i,u}\}$ from the sample covariance of this matrix after spatial smoothing.

Let $\{\hat{\mu}_{i,u}, \hat{\nu}_{i,u}\}_{i=1}^{\hat{L}_u}$ denote the spatial frequencies returned by 2D-ESPRIT, and define the virtual-array spatial frequency constant $\kappa_v \triangleq 2\pi d_v / \lambda$. Under the adopted virtual-array indexing, the spatial frequencies are related to the AoD by $\mu_{i,u} = \kappa_v \sin \theta_{i,u} \sin \phi_{i,u}$ and $\nu_{i,u} = -\kappa_v \cos \theta_{i,u}$. The minus sign in $\nu_{i,u}$ follows from the phase convention in (46) together with the chosen indexing along the z -direction of the virtual UPA. We focus on BS-side departures in the front half-space, i.e., $\phi_{i,u} \in [-\pi/2, \pi/2]$. The AoD angles are then recovered on the principal branches as

$$\hat{\theta}_{i,u} = \arccos\left(-\frac{\hat{\nu}_{i,u}}{\kappa_v}\right), \quad \hat{\phi}_{i,u} = \arcsin\left(\frac{\hat{\mu}_{i,u}}{\sqrt{\kappa_v^2 - \hat{\nu}_{i,u}^2}}\right), \quad (47)$$

where $\hat{\theta}_{i,u} \in [0, \pi]$ and $\hat{\phi}_{i,u} \in [-\pi/2, \pi/2]$ by construction. Numerically, the arguments of $\arccos(\cdot)$ and $\arcsin(\cdot)$ are clipped to their feasible intervals before inversion. This mapping is one-to-one over the front half-space when $d_v \leq \lambda/2$. For $d_v > \lambda/2$, we retain the same principal-branch inversion, while global uniqueness is not claimed.

With the estimated AoD pairs $\{(\hat{\theta}_{i,u}, \hat{\phi}_{i,u})\}$, the estimated direction vector is $\hat{\mathbf{k}}_{\text{tx},i,u} = [\sin \hat{\theta}_{i,u} \cos \hat{\phi}_{i,u}, \sin \hat{\theta}_{i,u} \sin \hat{\phi}_{i,u}, \cos \hat{\theta}_{i,u}]^T$. The steering matrix $\hat{\mathbf{B}}_{u,m} \in \mathbb{C}^{\hat{L}_u \times \hat{L}_u}$ is then assembled at any desired position \mathbf{p}_m via $[\hat{\mathbf{b}}_{u,m}]_i = e^{-j \frac{2\pi}{\lambda} \hat{\mathbf{k}}_{\text{tx},i,u}^T \mathbf{p}_m}$ (cf. Section II-B), and the basis-function matrix $\hat{\boldsymbol{\Omega}}_u \in \mathbb{R}^{\hat{L}_u \times K}$ is constructed as $[\hat{\boldsymbol{\Omega}}_u]_{i,k} = \omega_k(\hat{\theta}_{i,u}, \hat{\phi}_{i,u})$ (cf. Section II-C).

3) *Equivalent Channel Gain Estimation and eCSI Reconstruction*: Mirroring (8), define $\tilde{\chi}_{u,g} \in \mathbb{C}^{\hat{L}_u}$ as the equivalent path-gain vector under the estimated parametric model. The reconstructed eCSI then satisfies $\hat{\mathbf{q}}_{u,m,g}^H = \tilde{\chi}_{u,g}^H \hat{\mathbf{B}}_{u,m} \hat{\boldsymbol{\Omega}}_u$, where only $\hat{\mathbf{B}}_{u,m}$ depends on \mathbf{p}_m .

Accordingly, each virtual observation satisfies

$$\hat{h}_{u,m,g}^{(s)*} = \boldsymbol{\alpha}_{\text{ce}}^T \hat{\boldsymbol{\Omega}}_u^T \hat{\mathbf{B}}_{u,m}^{(s)H} \tilde{\chi}_{u,g}, \quad \forall m, s, \quad (48)$$

where $\hat{\mathbf{B}}_{u,m}^{(s)}$ is evaluated at the observation position $\mathbf{p}_m^{(s)}$. Concatenating all $N_s M$ observations into a single linear

Algorithm 3: Movement-aided parametric CE for SEMRA

Input: Uplink pilot observations $\{y_{u,m,g_j}^{(s)}\}_{u,m,j,s=1}^{U,M,J,N_s}$ and CE configuration (preselected CE pattern, pilot symbols/subcarrier allocation, and observation-position schedule).
Output: Estimated position-dependent eCSI model.

- 1 Generate the observation positions $\mathbf{p}_m^{(s)}$ via (43), $\forall m, s$;
- 2 **for** $u = 1$ **to** U **do**
- 3 Pilot normalization and stacking: form \mathbf{Y}_d from $\{y_{u,m,g_j}^{(s)}\}$;
- 4 Model-order estimation: obtain \hat{L}_u via MDL on $\mathbf{Y}_d \mathbf{Y}_d^H$ [34];
- 5 Delay estimation: estimate $\{\hat{\tau}_{i,u}\}_{i=1}^{\hat{L}_u}$ via 1D-ESPRIT;
- 6 sCSI recovery: reconstruct $\{\hat{h}_{u,m,g}^{(s)}\}$ at the virtual-array positions by delay-domain LS fitting;
- 7 Spatial-frequency estimation: re-index the recovered sCSI on the virtual array and estimate $\{(\hat{\mu}_{i,u}, \hat{\nu}_{i,u})\}_{i=1}^{\hat{L}_u}$ via 2D-ESPRIT;
- 8 AoD recovery: obtain $\{(\hat{\theta}_{i,u}, \hat{\phi}_{i,u})\}_{i=1}^{\hat{L}_u}$ via (47);
- 9 Basis and steering construction: build $\hat{\boldsymbol{\Omega}}_u$ and the steering matrices at the observation positions;
- 10 Equivalent-gain estimation: assemble $\boldsymbol{\Upsilon}_u$ and estimate $\tilde{\chi}_{u,g}$ via (50), for all g ;
- 11 Optional eCSI assembly: reconstruct $\hat{\mathbf{q}}_{u,m,g}$ at target positions via (51);
- 12 **end**
- 13 **return** estimated position-dependent eCSI model;

system gives $\hat{\mathbf{h}}_{u,g}^* = \boldsymbol{\Upsilon}_u \tilde{\chi}_{u,g}$, with the observation vector $\hat{\mathbf{h}}_{u,g}^* \in \mathbb{C}^{N_s M}$ and the measurement matrix

$$\boldsymbol{\Upsilon}_u \triangleq [\hat{\mathbf{B}}_{u,1}^{(1)} \hat{\boldsymbol{\Omega}}_u \boldsymbol{\alpha}_{\text{ce}}, \dots, \hat{\mathbf{B}}_{u,M}^{(N_s)} \hat{\boldsymbol{\Omega}}_u \boldsymbol{\alpha}_{\text{ce}}]^H \in \mathbb{C}^{N_s M \times \hat{L}_u}. \quad (49)$$

Provided that the columns of $\boldsymbol{\Upsilon}_u$ induced by the recovered paths are linearly independent, the matrix $\boldsymbol{\Upsilon}_u$ has full column rank. This requires nondegenerate steering responses over the $N_s M$ observation positions, a nonzero CE-pattern response on every recovered path, and $N_s M \geq \hat{L}_u$. Under this condition, the LS solution is

$$\hat{\chi}_{u,g} = (\boldsymbol{\Upsilon}_u^H \boldsymbol{\Upsilon}_u)^{-1} \boldsymbol{\Upsilon}_u^H \hat{\mathbf{h}}_{u,g}^*, \quad \forall g. \quad (50)$$

The eCSI at any target position \mathbf{p}_m then follows from

$$\hat{\mathbf{q}}_{u,m,g}^H = \hat{\chi}_{u,g}^H \hat{\mathbf{B}}_{u,m} \hat{\boldsymbol{\Omega}}_u, \quad \forall m, g, \quad (51)$$

where $\hat{\mathbf{B}}_{u,m}$ is evaluated at the target position, either the reference position $\bar{\mathbf{p}}_m$ or the optimized position from Sections III-IV. Because only $\hat{\mathbf{B}}_{u,m}$ depends on \mathbf{p}_m , the CE-phase observation positions and the data-transmission positions need not coincide.

This CE procedure uses $N_s = 4$ pilot slots with J pilots per slot per UE, for a total per-user pilot overhead of $N_s J$ symbols. For fair comparison, the EMRA baseline uses $T = N_s$ pattern-diversity slots, a preselected unit-norm training-pattern set, and the same J pilot subcarriers per UE per slot, yielding the same total per-user pilot overhead $N_s J$.

Overall, the proposed CE procedure uses multi-slot antenna repositioning to synthesize a virtual array and estimate a position-dependent parametric eCSI model. This model supports the target-position eCSI assembly required by the subsequent transmission design. The full pipeline is summarized in Algorithm 3.

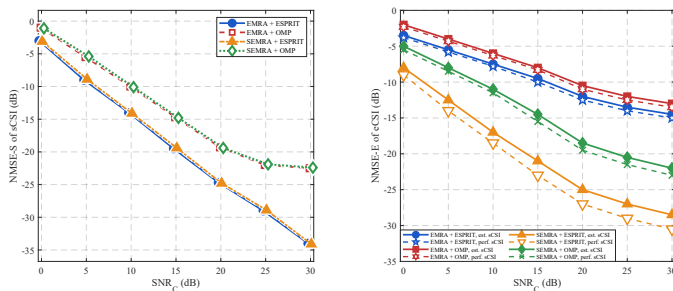


Fig. 4. Stage-wise NMSE-S and NMSE-E versus SNR_C at $d = \lambda/2$ for the EMRA baseline and the proposed SEMRA CE scheme.

VI. SIMULATION RESULTS

A. Simulation Setup

We simulate a TDD multiuser OFDM downlink with $f_c = 2.4$ GHz, $\Delta f = 30$ kHz, and $G = 128$ subcarriers. The BS uses a 4×4 reference UPA ($M = 16$), serves $U = 3$ single-antenna UEs, and employs $K = 10^2$ EM-domain basis functions. The multipath channel follows Section II-B and [32] with $L_u = 6$ paths per user and a nominal root-mean-square (RMS) delay spread of $\sigma_\tau = 100$ ns. During CE, each antenna visits $N_s = 4$ observation positions, forming an 8×8 virtual UPA with default spacing $d_v = d/2 = \lambda/4$. With guard distance $D_{\text{sep}} = \lambda/10$, the default displacement bound is $D_{\text{max}} = (d - D_{\text{sep}})/2 = \lambda/5$ at $d = \lambda/2$ and varies with d in the spacing sweep. A comb-type pilot allocation with $J = 30$ pilot subcarriers per user per slot is used.

The CE and precoding SNRs, denoted by SNR_C and SNR_P , are swept from 0 to 30 dB with default value 20 dB, and $N_{\text{max}} = 10$ unless otherwise stated. We compare SEMRA-ZF and SEMRA-WMMSE with EMRA and with TFA/SMA baselines using downtilt, 3GPP 38.901, and isotropic patterns. EMRA and SEMRA are reported under both estimated and perfect eCSI, TFA/SMA under perfect sCSI, and all results are averaged over 1000 channel realizations.

B. Channel Estimation Accuracy

We evaluate CE with $\text{NMSE-S} \triangleq \frac{\sum_{u,m,g,s} |\hat{h}_{u,m,g}^{(s)} - h_{u,m,g}^{(s)}|^2}{\sum_{u,m,g,s} |h_{u,m,g}^{(s)}|^2}$ at each scheme's CE positions and $\text{NMSE-E} \triangleq \frac{\sum_{u,m,g} \|\hat{\mathbf{q}}_{u,m,g} - \mathbf{q}_{u,m,g}\|_2^2}{\sum_{u,m,g} \|\mathbf{q}_{u,m,g}\|_2^2}$ on a common reference array. Both EMRA and SEMRA use the same per-user pilot overhead $N_s J = 120$; OMP benchmarks are included in addition to the ESPRIT-based pipeline following [15]. Thus, NMSE-S diagnoses the delay/sCSI stage, whereas NMSE-E, evaluated with either estimated or oracle sCSI input, measures the eCSI quality most relevant to tri-domain precoding.

Fig. 4 shows both metrics versus SNR_C at $d = \lambda/2$. For NMSE-S, the EMRA and SEMRA curves almost overlap for each algorithm, since this metric is dominated by the frequency-domain delay estimation and LS-based sCSI recovery rather than by spatial sampling density. ESPRIT keeps improving with SNR_C , whereas OMP saturates near -22.5 dB because of dictionary resolution. For NMSE-E, SEMRA+ESPRIT reaches about -28.5 dB at 30 dB, compared

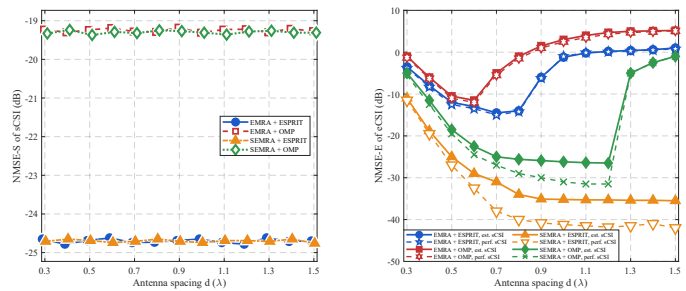


Fig. 5. Stage-wise NMSE-S and NMSE-E versus inter-element spacing d/λ at $\text{SNR}_C = 20$ dB for the EMRA baseline and the proposed SEMRA CE scheme.

with about -14.5 dB for EMRA+ESPRIT. The OMP benchmarks follow the same qualitative ordering, with SEMRA still outperforming EMRA, although with a smaller margin than ESPRIT. This separation is consistent with the CE pipeline in Section V, where antenna movement does not directly improve frequency-domain sCSI recovery; instead, the denser virtual array formed from the recovered sCSI enables more reliable AoD estimation and hence more accurate eCSI reconstruction.

Fig. 5 studies spacing sensitivity at $\text{SNR}_C = 20$ dB. For NMSE-S, the curves are nearly horizontal because changing the array spacing does not significantly alter the frequency-domain delay/sCSI recovery. For NMSE-E, the behavior is more geometry-dependent, with EMRA+ESPRIT bottoming out near $d = 0.7\lambda$ but degrading to about 1 dB at $d = 1.5\lambda$ due to principal-branch ambiguity and grating lobes. In contrast, SEMRA+ESPRIT is already about -25 dB at $d = 0.5\lambda$ and remains below -34 dB over the large-spacing region. Therefore, the spacing sweep reveals a clear aperture-ambiguity tradeoff for the fixed EMRA array, while the denser virtual sampling of SEMRA mitigates the large-spacing degradation in eCSI reconstruction.

C. Spectral Efficiency

Unless otherwise stated, the SE plots compare EMRA, SEMRA-ZF, and SEMRA-WMMSE under perfect and estimated eCSI, with TFA/SMA baselines under perfect sCSI. EMRA versus SEMRA-ZF isolates the spatial-reconfiguration gain under normalized ZF, while SEMRA-WMMSE shows the additional digital-domain gain; estimated-eCSI curves use the ESPRIT-based CE pipeline and $\text{SNR}_P = 20$ dB by default.

1) *SE versus SNR_C* : Fig. 6 plots SE versus SNR_C . All estimated-eCSI curves increase with SNR_C and approach their perfect-eCSI benchmarks, while the ordering SEMRA-WMMSE > SEMRA-ZF > EMRA is maintained over the whole range. The improvement is especially visible for EMRA, whose estimated-eCSI SE rises from the low-SNR regime but still remains below the SEMRA curves at high SNR_C . At $\text{SNR}_C = 20$ dB, the SEMRA perfect-versus-estimated gaps remain within about 0.5 bps/Hz, much smaller than the EMRA gap, which is consistent with the lower NMSE-E in Fig. 4. The remaining SEMRA-ZF gain under perfect eCSI confirms that spatial reconfiguration improves SE beyond CE accuracy alone, while SEMRA-WMMSE further benefits from stronger digital precoding.

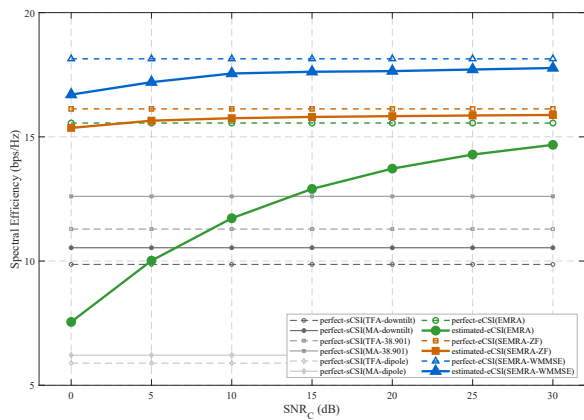


Fig. 6. Sum SE versus SNR_C when $\text{SNR}_P = 20$ dB and $d = \lambda/2$.

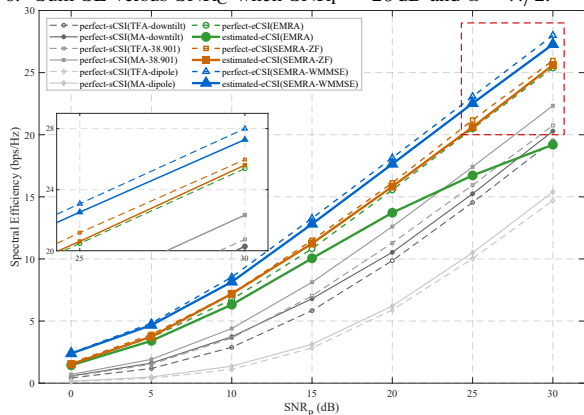


Fig. 7. Sum SE versus SNR_P when $\text{SNR}_C = 20$ dB and $d = \lambda/2$.

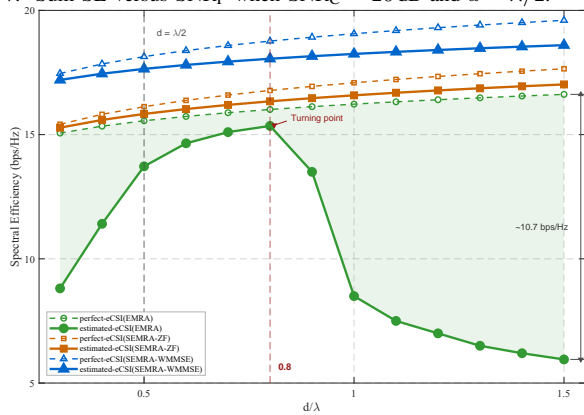


Fig. 8. Sum SE versus inter-element spacing d/λ when $\text{SNR}_C = 20$ dB and $\text{SNR}_P = 20$ dB.

2) *SE versus SNR_P* : Fig. 7 shows SE versus SNR_P at $\text{SNR}_C = 20$ dB. All curves increase approximately linearly with SNR_P , and the SEMRA advantage over EMRA persists across the entire range. At the default $\text{SNR}_P = 20$ dB, SEMRA-WMMSE achieves about 17.6 bps/Hz under estimated eCSI, compared with about 13.7 bps/Hz for EMRA and below-13 bps/Hz values for the fixed-pattern TFA/SMA baselines. The smaller perfect-versus-estimated gaps of the two SEMRA schemes again reflect their more accurate eCSI, while the persistent WMMSE-over-ZF gap, about 1.7 bps/Hz at high SNR_P , shows the benefit of the stronger digital design.

3) *SE versus Antenna Spacing*: Fig. 8 examines the impact of spacing when both SNRs are fixed at 20 dB. Varying d

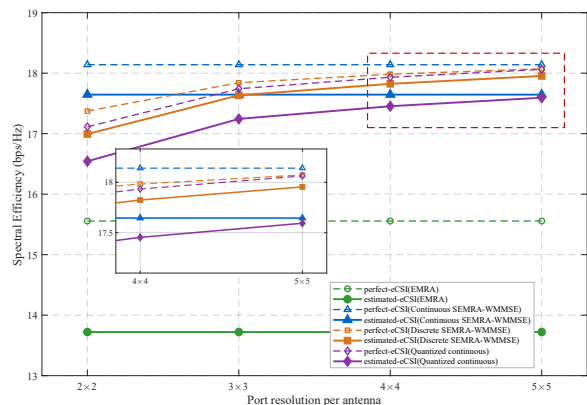


Fig. 9. Sum SE versus per-antenna port resolution $N \times N$ at $\text{SNR}_C = 20$ dB, $\text{SNR}_P = 20$ dB, and $d = \lambda/2$.

jointly changes the physical aperture, CE-side aliasing behavior, and, for SEMRA, the feasible motion region. The perfect-eCSI curves increase with d , reflecting the aperture gain available without estimation errors. Under estimated eCSI, EMRA first benefits from aperture enlargement and peaks at about 15.4 bps/Hz around $d \approx 0.8\lambda$, but then collapses to about 6.0 bps/Hz at $d = 1.5\lambda$, leaving the marked gap of about 10.7 bps/Hz to its perfect-eCSI counterpart. This SE turning point is slightly later than the NMSE-E minimum near 0.7λ in Fig. 5, because the additional aperture gain from 0.7λ to 0.8λ still compensates for the mild eCSI degradation. Once d grows further, principal-branch ambiguity and grating lobes dominate, so the EMRA estimated-eCSI SE drops sharply despite the larger aperture. By contrast, SEMRA-ZF and SEMRA-WMMSE increase monotonically with d and remain close to their perfect-eCSI benchmarks because SEMRA maintains low eCSI NMSE over the large-spacing region. At $d = 1.5\lambda$, their estimated-eCSI SEs are about 17.0 and 18.6 bps/Hz, respectively, confirming SEMRA's stronger robustness to enlarged inter-element spacings.

4) *SE versus Antenna Port Resolution*: In practice, antenna positions may be limited to mechanically realizable ports. We therefore restrict each antenna to an $N \times N$ uniform port grid inside \mathcal{S}_m and compare three SEMRA-WMMSE variants, namely the continuous PGD design, a discrete best-port sweep over the N^2 candidates inside Algorithm 2, and a quantized-continuous design that projects the continuous solution to the nearest port without re-optimization.

Fig. 9 shows that the discrete design rapidly approaches the continuous SEMRA-WMMSE benchmark as N increases. In particular, increasing the grid from $N = 2$ to $N = 3$ raises the estimated-eCSI SE from about 17.0 to 17.6 bps/Hz, essentially matching the continuous design and clearly outperforming the EMRA reference at about 13.7 bps/Hz. The quantized-continuous variant follows the same trend but stays slightly below the discrete re-optimized design, especially at coarse resolution. Additional ports provide only marginal refinement, so nine ports per antenna already capture nearly all continuous spatial-domain gain.

VII. CONCLUSIONS

This paper proposed a novel tri-domain MIMO with SEMRA for multiuser OFDM downlink over frequency-selective channels, where we jointly exploiting EM-domain pattern reconfigurability, spatial antenna movement, and digital precoding for enhanced performance. We formulated the corresponding tri-domain SE maximization problem, developed a ZF-based baseline to decouple the spatial-reconfiguration design, and proposed a WMMSE-based design for further improving the SE. To support these transmission designs under estimated CSI, we further developed a movement-aided parametric CE scheme that synthesizes a denser virtual array across pilot slots and improves AoD-driven eCSI reconstruction under the same per-user pilot overhead as EMRA. Simulation results showed that SEMRA improves eCSI estimation accuracy and achieves higher SE than EMRA, with SEMRA-WMMSE consistently outperforming SEMRA-ZF. The gains become more pronounced at larger inter-element spacings, where EMRA suffers from eCSI degradation, whereas SEMRA remains close to its perfect-eCSI benchmark. With a discrete per-antenna port codebook, it was shown that a 3×3 grid already recovers nearly all of the continuous SEMRA-WMMSE gain, demonstrating robustness to practical position discretization.

REFERENCES

- [1] Z. Wang, J. Zhang, H. Du, D. Niyato, S. Cui, B. Ai, M. Debbah, K. B. Letaief, and H. V. Poor, "A tutorial on extremely large-scale MIMO for 6G: Fundamentals, signal processing, and applications," *IEEE Commun. Surveys Tuts.*, vol. 26, no. 3, pp. 1560–1605, 2024.
- [2] T. Gong, P. Gavrilidis, R. Ji, C. Huang, G. C. Alexandropoulos, L. Wei, Z. Zhang, M. Debbah, H. V. Poor, and C. Yuen, "Holographic MIMO communications: Theoretical foundations, enabling technologies, and future directions," *IEEE Commun. Surveys Tuts.*, vol. 26, no. 1, pp. 196–257, 2024.
- [3] M. Di Renzo, A. Zappone, M. Debbah, M.-S. Alouini, C. Yuen, J. de Rosny, and S. A. Tretyakov, "Smart radio environments empowered by reconfigurable intelligent surfaces: How it works, state of research, and the road ahead," *IEEE J. Sel. Areas Commun.*, vol. 38, no. 11, pp. 2450–2525, 2020.
- [4] Q. Wu, S. Zhang, B. Zheng, C. You, and R. Zhang, "Intelligent reflecting surface-aided wireless communications: A tutorial," *IEEE Trans. Commun.*, vol. 69, no. 5, pp. 3313–3351, May 2021.
- [5] I. Krikidis, C. Psomas, A. Kumar Singh, and K. Jamieson, "Optimizing configuration selection in reconfigurable-antenna MIMO systems: Physics-inspired heuristic solvers," *IEEE Trans. Commun.*, vol. 72, no. 12, pp. 8010–8023, 2024.
- [6] K.-K. Wong and K.-F. Tong, "Fluid antenna multiple access," *IEEE Trans. Wireless Commun.*, vol. 21, no. 7, pp. 4801–4815, 2022.
- [7] L. Zhu, W. Ma, B. Ning, and R. Zhang, "Movable-antenna enhanced multiuser communication via antenna position optimization," *IEEE Trans. Wireless Commun.*, vol. 23, no. 7, pp. 7214–7229, Jul. 2024.
- [8] L. Zhu, W. Ma, W. Mei, Y. Zeng, Q. Wu, B. Ning, Z. Xiao, X. Shao, J. Zhang, and R. Zhang, "A tutorial on movable antennas for wireless networks," *IEEE Commun. Surveys Tuts.*, vol. 28, pp. 3002–3054, 2026.
- [9] W. K. New, K.-K. Wong, H. Xu, C. Wang, F. R. Ghadi, J. Zhang, J. Rao, R. Murch, P. Ramirez-Espinosa, H. Xiong, C.-B. Chae, and K.-F. Tong, "A tutorial on fluid antenna system for 6G networks: Encompassing communication theory, optimization methods and hardware designs," *IEEE Commun. Surveys Tuts.*, vol. 27, no. 4, pp. 2325–2377, Aug. 2025.
- [10] W. Ma, L. Zhu, Y. Tan, B. Zheng, Y. Zhang, Y. Zhang, K. Ying, Z. Gao, H. Sun, X. Shao, Z. Xiao, D. Niyato, and R. Zhang, "A survey on reconfigurable and movable antennas for wireless communications and sensing," *IEEE Commun. Surveys Tuts.*, vol. 28, pp. 4842–4882, 2026.
- [11] M. Hasan, I. Bahceci, and B. A. Cetiner, "Downlink multi-user MIMO transmission for radiation pattern reconfigurable antenna systems," *IEEE Trans. Wireless Commun.*, vol. 17, no. 10, pp. 6448–6463, Oct. 2018.
- [12] I. Bahceci, M. Hasan, T. M. Duman, and B. A. Cetiner, "Efficient channel estimation for reconfigurable MIMO antennas: Training techniques and performance analysis," *IEEE Trans. Wireless Commun.*, vol. 16, no. 1, pp. 565–580, Jan. 2017.
- [13] H. Wang, A. Li, Y.-F. Liu, Q. Qin, L. Song, and Y. Li, "Achievable rate maximization pattern design for reconfigurable MIMO antenna array," *IEEE Trans. Wireless Commun.*, vol. 22, no. 9, pp. 5884–5897, Sep. 2023.
- [14] T. Zhao, M. Li, and Y. Pan, "Online learning-based reconfigurable antenna mode selection exploiting channel correlation," *IEEE Trans. Wireless Commun.*, vol. 20, no. 10, pp. 6820–6834, 2021.
- [15] K. Ying, Z. Gao, Y. Su, T. Qin, M. Matthaiou, and R. Schober, "Reconfigurable massive MIMO: Precoding design and channel estimation in the electromagnetic domain," *IEEE Trans. Commun.*, vol. 73, no. 5, pp. 3423–3440, May 2025.
- [16] M. Liang and A. Li, "Deep learning-based channel extrapolation for pattern reconfigurable massive MIMO," *IEEE Trans. Veh. Technol.*, vol. 73, no. 3, pp. 4395–4400, Mar. 2024.
- [17] Z. Gao, L. Dai, Z. Lu, C. Yuen, and Z. Wang, "Super-resolution sparse MIMO-OFDM channel estimation based on spatial and temporal correlations," *IEEE Commun. Lett.*, vol. 18, no. 7, pp. 1266–1269, Jul. 2014.
- [18] A. Liao, Z. Gao, H. Wang, S. Chen, M.-S. Alouini, and H. Yin, "Closed-loop sparse channel estimation for wideband millimeter-wave full-dimensional MIMO systems," *IEEE Trans. Commun.*, vol. 67, no. 12, pp. 8329–8345, Dec. 2019.
- [19] B. Wang, F. Gao, S. Jin, H. Lin, and G. Y. Li, "Spatial- and frequency-wideband effects in millimeter-wave massive MIMO systems," *IEEE Trans. Signal Process.*, vol. 66, no. 13, pp. 3393–3406, Jul. 2018.
- [20] M. P. D. Costa, A. Richter, and V. Koivunen, "Unified array manifold decomposition based on spherical harmonics and 2-D Fourier basis," *IEEE Trans. Signal Process.*, vol. 58, no. 9, pp. 4634–4645, 2010.
- [21] Q.-U.-A. Nadeem, A. Kammoun, M. Debbah, and M.-S. Alouini, "A generalized spatial correlation model for 3D MIMO channels based on the Fourier coefficients of power spectrums," *IEEE Trans. Signal Process.*, vol. 63, no. 14, pp. 3671–3686, 2015.
- [22] S. Yang, Z. Wan, Y. Xiu, B. Ning, Y. Li, Y. Liu, and C. Yuen, "Flexible WMMSE beamforming for MU-MIMO movable antenna communications," *IEEE Trans. Signal Process.*, vol. 73, pp. 4479–4491, 2025.
- [23] Z. Xiao, X. Pi, L. Zhu, X.-G. Xia, and R. Zhang, "Multiuser communications with movable-antenna base station: Joint antenna positioning, receive combining, and power control," *IEEE Trans. Wireless Commun.*, vol. 23, no. 12, pp. 19744–19759, Dec. 2024.
- [24] L. Zhu, W. Ma, and R. Zhang, "Movable-antenna array enhanced beamforming: Achieving full array gain with null steering," *IEEE Commun. Lett.*, vol. 27, no. 12, pp. 3340–3344, Dec. 2023.
- [25] X. Shao, Q. Jiang, and R. Zhang, "6D movable antenna based on user distribution: Modeling and optimization," *IEEE Trans. Wireless Commun.*, vol. 24, no. 1, pp. 355–370, Jan. 2025.
- [26] C. Skouroumounis and I. Krikidis, "Fluid antenna with linear MMSE channel estimation for large-scale cellular networks," *IEEE Trans. Commun.*, vol. 71, no. 2, pp. 1112–1125, Feb. 2023.
- [27] Z. Zhang, J. Zhu, L. Dai, and J. R. W. Heath, "Successive Bayesian reconstructor for channel estimation in fluid antenna systems," *IEEE Trans. Wireless Commun.*, vol. 24, no. 3, pp. 1992–2006, Mar. 2025.
- [28] Y. Zhou, H. Hua, J. Xu, and R. Zhang, "Two-timescale optimization for hybrid mechanically and electronically tunable 6DMA aided communication," *IEEE Wireless Commun. Lett.*, vol. 15, pp. 2050–2054, 2026.
- [29] J. Zhang, J. Rao, Z. Li, Z. Ming, C.-Y. Chiu, K.-K. Wong, K.-F. Tong, and R. Murch, "A novel pixel-based reconfigurable antenna applied in fluid antenna systems with high switching speed," *IEEE Open J. Antennas Propag.*, vol. 6, no. 1, pp. 212–228, 2025.
- [30] K. Chen, C. Qi, Y. Hong, and C. Yuen, "REMAA: Reconfigurable pixel antenna-based electronic movable-antenna arrays for multiuser communications," *IEEE Trans. Commun.*, vol. 73, no. 11, pp. 12913–12928, Nov. 2025.
- [31] Y. Li, C. Qi, S. Mao, and O. A. Dobre, "Tri-hybrid beamforming for radiation-center reconfigurable antenna array: Spectral efficiency and energy efficiency," *IEEE Trans. Wireless Commun.*, vol. 25, no. 1, pp. 1–16, Jan. 2026.
- [32] "Study on Channel Model for Frequencies From 0.5 to 100 GHz," document TR 38.901, 05, Version 14.0.0, 3GPP, 2017.
- [33] Q. Shi, M. Razaviyayn, Z.-Q. Luo, and C. He, "An iteratively weighted MMSE approach to distributed sum-utility maximization for a MIMO interfering broadcast channel," *IEEE Trans. Signal Process.*, vol. 59, no. 9, pp. 4331–4340, 2011.
- [34] M. Wax and T. Kailath, "Detection of signals by information theoretic criteria," *IEEE Trans. Acoust., Speech, Signal Process.*, vol. 33, no. 2, pp. 387–392, Apr. 1985.